Interfacial & Nanoscale Science Facility

The Interfacial & Nanoscale Science (I&NS) Facility is a world-class resource for scientific expertise and instrumentation related to the study of interfacial phenomena and nanoscience and technology. This section summarizes the capabilities that exist in the I&NS Facility, along with research programs associated with facility users. Activities in the I&NS Facility address national needs in environmental restoration, waste management, pollution prevention, energy, and national security through research that specializes in preparation, characterization, interactions, and reactivity of interfaces and nanoscale materials. The range of scientific expertise and instrumentation within the I&NS Facility provides a unique environment for research in areas such as nanoscience and nanotechnology; heterogeneous catalysis; environmental interfaces including aerosols and minerals; materials and chemoselective interfaces; and areas within microanalytical science such as chemical sensing and nanobiotechnology.

The I&NS Facility and its scientific staff provide a broad range of instrumentation, laboratory capabilities, and expertise. Instrumentation is available for chemical synthesis, analytical chemistry, separations, electrochemistry, thin film deposition, catalytic reactors, ion-beam processing, and microfabrication. Capabilities include an accelerator facility for material modification and analysis using ion beams along with interface characterization; scanning probe microscopies; electron microscopy and x-ray analysis; spectroelectrochemistry; high-spatial/energy resolution surface analysis; catalyst preparation, characterization, and reaction engineering; fully equipped clean room for microfabrication, microanalytical systems development and testing laboratories; inorganic, organic, polymer, and biochemical synthesis and characterization facilities; a full complement of thin-film deposition and characterization facilities; and fully equipped analytical support laboratories. The combination of surface and interface characterization techniques that provide high spatial, depth, and energy resolution for a broad array of methods is unmatched anywhere in the world. Many systems are coupled directly to film growth chambers, and samples can be moved among 16 different systems under controlled environment without exposure to air.

Instrumentation & Capabilities

- Thin-film deposition
- Surface analysis suite
- Electron microscopy suite
- Scanning probe microscopy
- Ion-beam processing and analysis
- Nanobiotechnology capabilities
- Surface science and catalysis laboratory
- Catalytic reactors
- X-ray diffraction laboratory
- Microfabrication
- Chemical and biological sensing
- Other analytical and characterization laboratories

I&NS Facility staff in collaboration with Pacific Northwest National Laboratory staff continue to focus on innovative research in the areas of surface and interfacial chemistry, advanced materials synthesis and characterization, and microanalytical science. Our activities emphasize research relevant to the four U.S. Department of Energy mission areas—science, energy resources, environmental quality, and national security—and to operation of a world-class user facility for scientific problem-solving that supports the science mission. Our staff also plays a major role in the continued success of the W.R. Wiley Environmental Molecular Sciences Laboratory (EMSL) by providing support, training, and collaboration to onsite users. Over the past five years, research activities in the I&NS Facility were concentrated in four major thrust areas: films and interphases, surface chemistry and catalysis, material interfaces, and microsensors and microfluidics. Staff within the I&NS Facility continue to focus their efforts in these four areas, with research on the following topics:

- **Oxide and Mineral Films and Surfaces**. Structural and chemical properties of model single-crystal oxide and complex mineral surfaces
- **Electronic and Catalytic Materials**. High dielectric materials, magnetic oxide semiconductors, and oxide catalysts
- **Nanoscale Materials**. Oxide quantum dots and nano films of magnetic and oxygen ion-conducting oxides, buried nanoclusters in oxides
- **Interfacial Properties and Reactivity**. Reactions at oxide and mineral interfaces and the structural and chemical properties
- **Microanalytical Separations and Sensing**. Development of new microanalytical and sensing principles, tools, and testing
- **Nanobiotechnology**. Single-enzyme nanoparticles, enzymes in nanostructured matrices, understanding the dynamics of these materials
- **Environmental Studies**. Waste separations, structural and chemical stability of waste forms under different radiation and chemical environment, atmospheric aerosols
- **Analysis and Characterization**. Fully equipped analytical laboratories and characterization facilities.

Films and Interphases. The physical and chemical properties of the region between single phases of material (the interphase) have a major influence on many characteristics of the material, including stability, electronic properties, atomic and ionic transport, and chemical reactivity. Research programs include the synthesis of thin films and nanostructured materials, both of which contain a high concentration of interphase regions. Research activities also involve studies of solid/solid, solid/liquid, and solid/gas (or vacuum) interphase regions. Although most studies are focused on inorganic materials and interphases, organic and biological systems are becoming an increasingly large part of our work.

Surface Chemistry and Catalysis. Basic research is carried out with the most simple, well-defined, environmentally relevant crystallographic structures (e.g., mineral carbonates, metal oxides) where molecular theory and spectroscopy are immediately applicable. The work then progresses to materials with more complex structures, such as iron and titanium oxides with substitutional impurities. For example, fundamental studies of the oxygen storage and release properties of pure and zirconium-doped ceria single-crystal thin films are aimed at understanding how these “oxygen storage materials” perform in an automobile exhaust catalytic converter. In addition to fundamental surface chemistry research, we are developing materials and reactor designs for a number of heterogeneous catalytic processes. One study involves synthesizing, characterizing, and testing a group of novel, mesoporous silica-supported, solid-acid catalysts for use in petroleum refining processes.

Material Interfaces. Studies are being conducted on solid/solid interfaces in a wide variety of materials, radiation effects in materials, fundamental defect properties and interactions, atomic and ionic transport, and aerosol characterization. Many of the studies on solid/solid interfaces involve 1) characterization of interfaces between thin films and substrates, between ion-beam-modified surfaces and the original substrate, or between nanoclusters and host matrices; 2) segregation or diffusion of point defects, impurities, dopants, or gas atoms to or away from such interfaces; 3) transport of hydrogen, oxygen, or other gases across such interfaces; 4) formation or destruction of such interfaces from radiation damage processes; and 5) stability of interfaces under a wide range of environmental conditions. Studies on radiation effects include experimental research on materials for immobilization of nuclear waste and plutonium, as well as materials for next-generation nuclear power production, wide-band-gap semiconductors, and multi-scale computer simulations of damage production processes, defect diffusion, and microstructure evolution. Studies on atomic and ionic transport include ion exchange processes in nuclear waste glasses, hydrogen storage and transport in materials, and oxygen transport in fast ion conductors.

Microsensors, Microfluids, and Nanobiotechnology. This research area includes four primary thrust areas: 1) array-based vapor sensors, 2) nanoscience, 3) bioanalytical microfluidics, and 4) radioanalytical microfluidics. Key areas of science in array-based vapor sensing include rational design and synthesis of polymeric sensing materials, linear free-energy models for vapor/polymer interactions, organic thin films, photopatterning methods for sensor materials, integrated sensor system development, and multi-variate data analysis. The nanoscience area includes development of monolayer-protected gold nanoparticles for use on sorptive sensing films, single-enzyme nanoparticles as a new nanostructure for enzyme stabilization, and multi-functional nanoparticle assemblies for biodetection. The latter two areas represent a new thrust in nanobiotechnology, and a laboratory within EMSL has been established for synthesizing enzyme nanostructures and studying enzyme kinetics and enzymes in nanostructured matrices. Experimental research in the latter two areas, bioanalytical microfliudics and radioanalytical microfluidics, is now located primarily in other facilities but close scientific ties with EMSL are maintained.

Major Capabilities in I&NS Facility

Thin Film Deposition. Thin film deposition capabilities include oxygen plasma-assisted molecular beam epitaxy (MBE) systems, a metal organic chemical vapor deposition system (MOCVD), and a sputter deposition system. The MBE systems consist of growth chambers connected to surface characterization chambers through sample transfer lines. The growth chambers have various electron beam and effusion cell sources along with reflection high-energy electron diffraction (RHEED) and quartz crystal oscillators to monitor the growth. The surface characterization chambers are equipped with several surface science capabilities including x-ray photoelectron spectroscopy (XPS)/diffraction (XPD), Auger electron spectroscopy (AES) low-energy electron diffraction (LEED), and atomic force microscopy/ scanning tunneling microscopy (AFM/STM). The MOCVD system is specially designed for epitaxial growth of oxide thin films. The system comprises a rotating disk reactor, two metal organic source delivery systems (bubbler vapor-phase and direct liquid source-injection), an oxygen microwave plasma unit, a spectroscopic ellipsometer, and a Fourier transform, infrared (FTIR) spectrometer. The system is capable of growing uniform (in both thickness and composition) oxide thin films with abrupt interfaces. The sputter deposition system consists of RF and DC sputtering sources.

Surface Analysis Suite. The surface analysis suite consists of a Physical Electronics Instruments (PHI) Quantum 2000 high-resolution, x-ray photoelectron spectrometer

Figure 1. X-Ray Photoelectron Spectrometer.

(pictured in Figure 1), a Kratos Axis multi-technique surface analysis system (SAS), a PHI Model T2100 time-of-flight secondary ion mass spectrometer (TOF-SIMS), and a PHI Model 680 Auger electron spectroscopy (AES)/scanning Auger microprobes. The Quantum 2000 XPS system is unique in that it uses a focused monochromatic Al K α x-ray beam that can be varied in size from as small as 10 μm in diameter to approximately 200 μm. The TOF-SIMS system uses a pulsed and focused ion source and TOF analyzer to obtain high spatial- and mass-resolution data from a specimen surface. The multi-technique SAS enables surfaces to be probed with a variety of complementary analysis methods, and contains electron imaging, electron spectroscopy, and both primary and secondary ion-scattering capabilities. The Model 680 AES/scanning Auger microprobes is based upon a field emission electron source and a cylindrical mirror analyzer. The electron beam size can be focused as low as 10 nm at 20 kV, although somewhat larger beams are typically used to collect AES data. Instrument features and capabilities include beam rastering, SEM imaging, mapping, a sputter gun for specimen cleaning and depth profiling, and sample rotation to allow “Zalar” rotation during sputtering. The system also is configured with an x-ray detector for near-surface analysis in combination with AES surface analysis.

Electron Microscopy Suite. The electron microscopy suite consists of a LEO 982 field emission scanning electron microscope (FESEM), high-resolution transmission electron microscope (TEM), and an environmental scanning electron microscope (ESEM). The FESEM is an ultra-high performance SEM with a resolution of 1 nm at 30 kV and 4 nm at 1.0 kV. It has a large specimen chamber equipped with multiple detectors: a below-lens secondary electron detector, an in-lens secondary electron detector, a backscatter electron detector, an energy dispersive x-ray detector, and a detector for electron backscatter diffraction. The JEOL 2010 is a high-resolution TEM with a spatial resolution of 0.194 nm. This instrument has a medium acceleration voltage of 200 kV, a high brightness electron source, digital image recording, a computer-controlled sample goniometer, and a geometrically optimized x-ray detector. It has a wide range of illumination lens conditions—TEM mode, energy dispersive spectroscopy mode, nanometer beam electron diffraction (NBED), and convergent beam electron diffraction (CBED). The TEM is post-column attached with a Gatan image filter, giving an optimized energy resolution of ~1.2 eV, enabling light element analysis by electron energy-loss spectroscopy (EELS) and elemental mapping in the electron spectroscopic imaging (ESI). The ESEM is a high-performance, variable-pressure SEM with a resolution of 5 nm at 30 kV. It can be used to examine uncoated, non-conductive specimens, and with a Peltier stage, it can be used with wet specimens. It will image specimens in a variety of atmospheres, such as water vapor, air, argon, nitrogen, and helium. The ESEM has a large specimen chamber equipped with an energy dispersive x-ray detector, a micro-injector, and a micromanipulator.

Scanning Probe Microscopy. The scanning probe microscopy laboratory has a Digital Instrument (DI) Nanoscope IIIa AFM, a Topometrix TMX 1000 Explorer SPM, and a Park-VP scanning probe microscope. The DI Nanoscope IIIa AFM is capable of operating in both air and liquid environments and in several modes that include contact, tapping, frictional force, phase/frequency, capacitance, and magnetic/electrostatic force. As a real space probe, the instrument can be used to probe surface morphology, defects, and electrostatic, magnetic, dopant concentration, and mechanical properties of conducting and non-conducting materials. The Topometrix TMX 1000 Explorer SPM can be used for both AFM and STM in air and in liquid and is particularly useful for larger samples. This instrument includes both contact and non-contact AFM modes. STM requires an electrically conductive sample and produces images based on the topography and electronic structure of the sample. AFM samples may be insulating or conducting; the image is based on the force between the AFM probe and the sample and is primarily a map of the surface topography. The Park-VP scanning probe microscope can be used for both STM and AFM in ultra-high vacuum (UHV) conditions. As a real space probe, this instrument is designed to probe surface structure, defects, and morphology of conducting and non-conducting materials. In addition to STM/AFM, the vacuum system also is equipped with other surface science capabilities that include LEED, XPS, AES, and oxygen plasma cleaning.

Ion Beam Processing and Analysis. The accelerator facility is equipped with capabilities to perform material modification and analysis using high energy ion beams. The facility has two ion sources, a 3 MeV tandem ion accelerator, injector and analyzing magnets, beam lines, and four end stations. The end station on the +30° beam line is equipped with LEED, AES, XPS, oxygen plasma, and sputter cleaning sources and effusion cells in addition to the conventional ion beam capabilities. Ion beam capabilities include fixed and movable detectors for Rutherford backscattering spectrometry/channeling (RBS/C), nuclear reaction analysis (NRA), and elastic recoil detection analysis (ERDA). This beam line extends through the end station to another end station where experiments can be performed with the beam size of 20 microns or greater. The micro-beam end station is also equipped with capabilities for conventional ion beam techniques including RBS, NRA, and proton induced x-ray emission (PIXE). The +15° beam line is equipped with a raster scanner for ion implantation and ion beam modification of materials, and the end station is equipped with all the conventional ion beam capabilities. The –15° end station is designed to carry out routine analytical work. An NEC RC 43 end station is attached to this beam line. This end station is equipped with most of the standard ion beam analytical capabilities including RBS, NRA, PIXE, particle induced gamma emission (PIGE), proton elastic scattering analysis, scanning transmission ion microscopy (STIM), and ERDA.

Surface Science and Catalysis Laboratory. Three UHV surface chemistry systems designed for studies of the molecular-level chemistry of adsorbates on metal oxide surfaces reside in the Surface Science and Catalysis Laboratory . These systems are equipped with a number of spectroscopic tools to follow changes in adsorbate chemistry, including high-resolution electron energy loss spectroscopy (HREELS), SIMS, ultraviolet photoemission (UPS), XPS, AES, and LEED. In addition, both electron-stimulated (ESD) and temperature-programmed desorption (TPD) studies are routinely performed in some systems. Typical information obtainable in TPD experiments includes the quantity and nature (intact or dissociated molecule) of an adsorbed gas. In addition, estimates of the sticking coefficient and the activation energy for desorption and/or reaction of the adsorbed molecule can be made. One of these systems has a combination of surface science and high-pressure catalysis capabilities and is capable of measuring gas/solid reaction rates under realistic, high-pressure (~1 atm) conditions using model, low surface area solid samples. Reaction rates as a function of temperature and varying reagent partial pressures also can be measured in this system.

Catalytic Reactors. The Reaction Engineering Laboratories are equipped with a variety of analytical capabilities and catalytic reactors including an RXM-100 multi-functional instrument and a Zeton Altamira reactor test stand. The RXM-100, a multi-functional instrument used for catalyst studies, combines UHV and high-pressure capabilities in a single instrument without compromising specifications or ease of use. A number of measurements can be made using this instrument including chemical adsorption, physical adsorption, BET surface area, pore size, pore distribution, and temperature programmed characterization (desorption, reduction, and oxidation). An on-line mass spectrometer, gas chromatograph, FTIR, and thermal conductivity detector can be used to analyze effluent gases. The instrument has the capability of running up to 10 different gases simultaneously. In addition, high-pressure reactions (up to 1000 psi) can be run within a few minutes of each other on the same system, with little change in system configuration. This system offers extensive flexibility in catalyst testing and decreases inefficiency and contamination problems that arise from transferring materials between systems and waiting for data from other sources. The Zeton Altamira reactor test stand comprises three types of reactors generally used in bench scale testing of catalysts: a fixed bed reactor, a Rotoberty reactor, and a continuous stirred tank reactor. This design allows users to evaluate catalyst performance and to study chemical reactions in various reactor configurations.

X-Ray Diffraction. The suite of x-ray diffraction (XRD) equipment in EMSL consists of four instruments: 1) a general-purpose XRD system for studying polycrystalline samples under ambient conditions, 2) a special applications XRD system with low- and high-temperature sample stages covering the range of -193°C to +1000°C, and 3) a four-circle XRD system. The general-purpose system is most often used to examine powder samples (x-ray powder diffraction [XRPD]), but can also be used to study certain types of thin films. In addition to its non-ambient capabilities, the special applications system is equipped to examine thin film samples in more detail, including grazing-incidence x-ray diffraction (GIXRD) and x-ray reflectivity (XRR) measurements. The four-circle system is typically configured for high-resolution x-ray diffraction (HRXRD) studies of epitaxial thin films. Additional applications of the four-circle system include stress measurements, texture analysis, GIXRD, and XRR.

Chemically Selective Materials and Sensors. The development and evaluation of sensor materials and chemical microsensors is supported by a wet chemistry laboratory for organic, polymer, and nanomaterial synthesis; a laboratory for evaluation of chemical sensor and sensor materials using automated vapor generation and blending systems; and a clean room with selected microfabrication capabilities. A variety of techniques for the application of sensing materials to sensor devices are available and numerous electronic test instruments are available in the sensing laboratories and the EMSL Instrument Development Laboratory. These capabilities are complemented by a range of surface analysis and characterization instruments as well as conventional analytical instrumentation in EMSL. Users may wish to bring new sensing materials to EMSL for application to sensing devices and evaluation, while others may bring complete sensor systems with data collection to couple to our automated vapor generation systems. Research areas include sensor arrays, sensor materials design and synthesis, sensing material/analyte interactions, and chemometric methods.

Microfabrication. Microfabrication equipment provides a significant research and development capability in the areas of microstructures, microsensors, and microanalytical systems. Unlike highly automated industrial production equipment, this microfabrication equipment is flexible and multi-purpose in function. The equipment supports a variety of microprocessing activities that include thin film deposition, thermal treatments, microphotolithography, chemical etching, inspection and characterization, bonding and packaging, and test and measurement.

Nanobiotechnology Laboratory. The Nanobiotechnology Laboratory is equipped with capabilities to synthesize single-enzyme nanoparticles, functionalize nanostructured matrices, and analyze the activity and stability of enzymes and single-enzyme nanoparticles. This new laboratory consists of various small instruments (such as a black box, a glove box, a Dean Stark system, and shakers), spectrophotometer, and spectrofluorometer. A variety of basic enzyme works can be performed in this laboratory, including enzyme modification, enzyme immobilization, and enzyme activity and stability measurement.

Upgrades

Sample Heating and Additional Sputter Disposition Capability. The large area growth chamber in the sputter deposition laboratory has been upgraded with a facility to grow thin films at substrate temperatures more than 1000°C in various reactive gases like oxygen and nitrogen. In addition, another 4-inch sputter gun, which could run on DC as well as in RF sputtering mode, was added to the chamber. This upgrade enhances the flexibility of this chamber and the co-sputtering capability.

Software and Hardware Enhancement for XRD Analysis. Software packages were acquired to facilitate simulation and fitting of specular and diffuse x-ray reflectivity data and dynamical, high-resolution rocking curves. The structure of unknown samples can be effectively modeled using these programs. In addition, a motorized alignment stage was added to the special applications XRD system. This shaft-type stage replaced the original and comparatively primitive block-type adapter, the use of which necessitated realignment of the system when changing between the TTK450 low-temperature camera and any of the other sample platforms integral with that system. A custom fixture for collection of high-resolution, x-ray topography images was also designed and built for the four-circle XRD system.

MBE Facility. Because of its level of use, the oxygen plasma assisted MBE system (OPA-MBE) was upgraded with additional effusion cells. With the additional effusion cells, the total number of individually controlled MBE sources is seven: four electron beams and three effusion cells. In addition, new vibrating sample magnetometer instrumentation was purchased and installed in the MBE laboratory for magnetic measurements. The vibrating sample magnetometer includes a cryostat and high-temperature oven options for measurements from 8 K to 1300 K, full 720-degree rotation, and vector coils for determination of anisotropies.

Enhancement of Sample Manipulation in Catalysis Chamber. The sample manipulation capability of the UHV surface chemistry/catalysis chamber in the Surface Science and Catalysis Laboratory was enhanced by adding a new 14-inch rotating platform and a new xyz stage with ± 1-inch x and y translations and a 24-inch z translation. In addition, an antichamber that will house the oxygen plasma source and metal deposition capabilities was also added.

In Situ Grazing-Incidence EXAFS Study of Pb(II) Chemisorption on Hematite (0001) and ($1\bar{1}02$) Surfaces

J Bargar,[a] T Trainor,[b,c] J Fitts,[b,d] S Chambers,[e] and G Brown, Jr.[a,b]
(a) Stanford Synchrotron Radiation Laboratory, Menlo Park, California
(b) Stanford University, Stanford, California
(c) University of Alaska, Fairbanks, Alaska
(d) Brookhaven National Laboratory, Upton, New York
(e) Pacific Northwest National Laboratory, Richland, Washington

Heavy-metal ion transport in natural waters is influenced by reactions between solute species and solid materials (e.g., mineral surfaces, humic materials, biomass). Adsorption of cations onto mineral surfaces is of major importance for heavy metal attenuation, even in biomass-rich systems. In particular, Fe- and Mn-oxides and (oxy)hydroxides are very common in the environment and have high sorptive capacities for metal ions in the pH ranges of most natural waters. The reactivity of a metal-oxide surface is controlled, in part, by the types and concentrations of surface sites exposed to aqueous solution. In addition, surface-site reactivity is a key factor in heterogeneous chemical processes such as catalysis, crystal growth, preparation of semiconductors, and energy storage in fuel cells. Little is known at present about the structure and composition of reactive sites on metal-oxide surfaces in contact with aqueous solutions, mostly because of the difficulty of probing such sites experimentally.

In this project, the structures of Pb(II) complexes adsorbed on two common hematite (α-Fe_2O_3) single-crystal surfaces [(0001) (C-cut) and ($1\bar{1}02$) (R-cut)] were studied using grazing-incidence (GI) x-ray absorption fine structure (XAFS) spectroscopy under *in situ* conditions (i.e., in the presence of bulk solution at ambient temperature and pressure) to obtain information on reactive surface sites to which Pb(II) preferentially binds and on the structure and composition of the Pb(II) surface complexes. The specimens were epitaxial films grown on sapphire substrates in the W.R. Wiley Environmental Molecular Sciences Laboratory (EMSL). Oligomeric Pb(II) complexes were found to bind in inner-sphere modes on both surfaces, which is in contrast with the binding of aqueous Pb(II) on α-Al_2O_3 (0001) surfaces where Pb(II) was found in previous GI-XAFS studies to bind in a dominantly outer-sphere mode, indicating a significant difference in reactivity of these two surfaces to Pb(II) (Bargar et al. 1997). This difference in reactivity to Pb(II) is explained on the basis of recent crystal truncation rod diffraction studies of the α-Fe_2O_3 and α-Al_2O_3 C-cut surfaces in contact with bulk water, which found major structural differences between the surfaces of these two metal oxides. The structures for the two hematite surfaces used in this study are shown in Figure 1, and the structural results are summarized in Table 1.

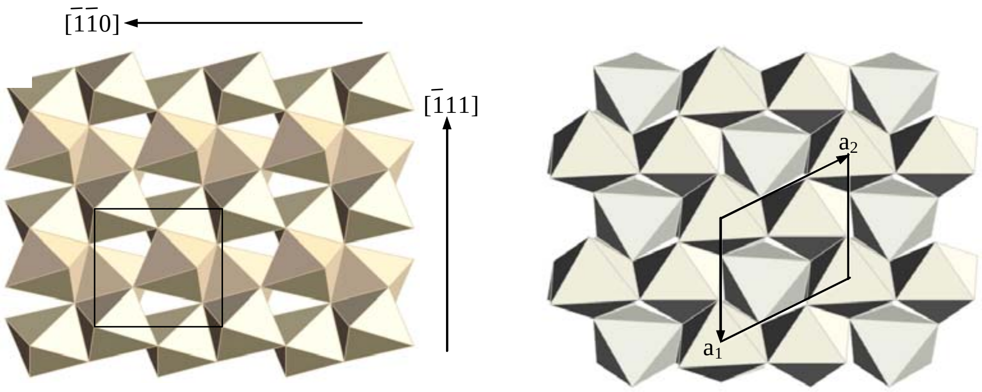

Figure 1. Left: Polyhedral representation of the oxygen-terminated R-cut surface. Surface unit cell is outlined in black. Surface unit cell edge lengths are 5.038 Å for the edge parallel to [110] and 5.435 Å for the edge parallel to [111] (c-axis projection). Right: Polyhedral representation of the oxygen-terminated hematite C-cut surface. Unit cell edge-length is 5.038 Å.

Table 1. X-Ray Photoelectron Spectroscopy (XPS) and EXAFS results.

Sample	XPS			EXAFS		
	Γ (atoms /nm^2)		O	O$_{aq}$$^{(a)}$	Fe	Pb
Pb(II)/(0001) (C-cut)		CN	2.5 (.1)	0.8	0.4 (.2)	2.8 (.6)
	8.3 (1.0)	R(Å)	2.24 (.01)	2.51	3.81 (.06)	3.62 (.03)
		σ^2 (Å^2)	0.01	0.01	0.01	0.01
Pb(II)/($1\bar{1}02$) (R-cut)		CN	2.0 (.2)	0.8 (.4)	0.4 - 0.6	2.9 (.6)
	7.2 (0.9)	R(Å)	2.280 (.007)	2.51	3.34 – 3.86	3.69 (.04)
		σ^2 (Å^2)	0.01	0.01	0.01	0.01
Pb(II)/Hematite powder, pH 7$^{(b)}$		CN	2.2 (.1)	--	0.5 (.1)	--
	1.2 - 6.0	R(Å)	2.28 (.01)	--	3.28 (.02)	--
		σ^2 (Å^2)	0.01	--	0.01	--

Explanation of table: Γ = sorption density, CN = coordination number, R = interatomic distance, σ^2= Debye-Waller factor. Estimated standard deviations are given in parentheses.

(a) This shell accounts for aqueous and outer-sphere species.

(b) From Bargar et al. (1998).

References

Bargar, JR, SN Towle, GE Brown Jr, GA Parks, and J Colloid. 1997. "XAFS and Bond-Valence Determination of the Structures and Compositions of Surface Functional Groups and Pb(II) and Co(II) Sorption Products on Single-Crystal α-Al_2O_3." *Journal of Colloid and Interface Sci* 185:473-492.

Bargar, JR, GE Brown Jr, and GA Parks. 1998. "Surface Complexation of Pb(II) at Oxide-Water Interfaces: III. XAFS Determination of Pb(II) and Pb(II)-chloro Adsorption Complexes on Geothite and Alumina." *Geochimica et Cosmochimica Acta* 62:193-207.

Defect Diffusion and Irradiation-Induced Recovery in 6H-SiC

W Jiang,[(a)] W Weber,[(a)] Y Zhang,[(b)] S Thevuthasan,[(b)] and V Shutthanandan[(b)]
(a) Pacific Northwest National Laboratory, Richland, Washington
(b) W.R. Wiley Environmental Molecular Sciences Laboratory, Richland, Washington

Polytypes of silicon carbide (SiC) possess many outstanding properties that make the material a prominent candidate for high-temperature, high-power, and high-frequency microelectronic and optoelectronic devices. While ion implantation is a crucial process for dopant incorporation in device fabrication, it inevitably produces lattice disorder that is detrimental to device performance and must be removed by subsequent annealing processes before the implants are rendered electrically active. SiC also has been proposed for structural components in fusion reactors and cladding materials for gas-cooled fission reactors, where high-temperature, high-radiation environments are involved. Performance prediction of SiC in these harsh environments is essential for safe and economical operations. Thus, a fundamental understanding of the accumulation and recovery of irradiation damage is needed to advance the utilization of SiC in these technological applications.

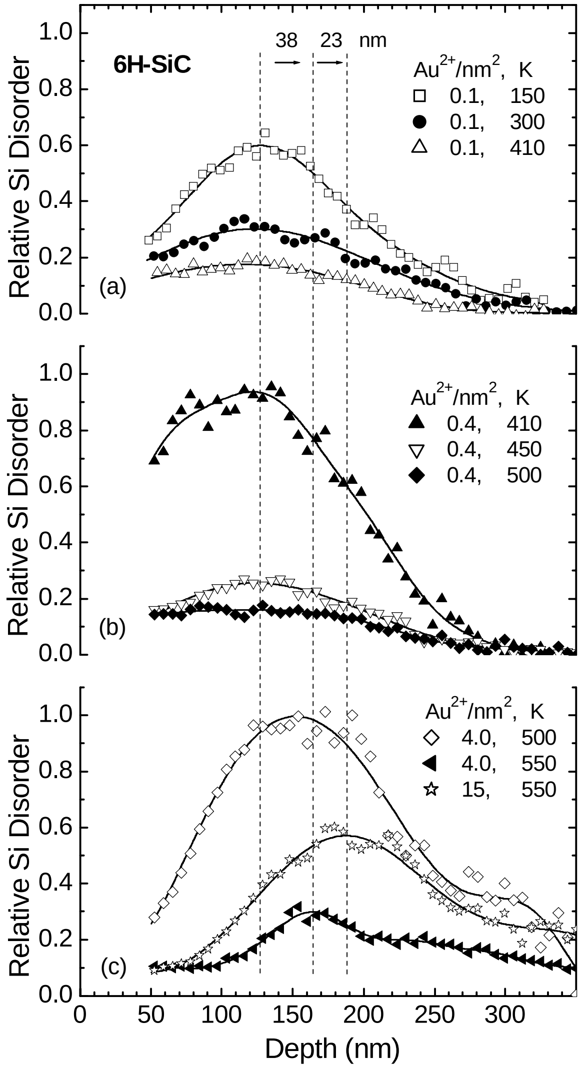

Figure 1. Depth profiles of relative Si disorder in 6H-SiC irradiated 60° off the surface normal with 2.0 MeV Au^{2+} ions at different temperatures to (a) 0.1 Au^{2+}/nm^2, (b) 0.4 Au^{2+}/nm^2, and (c) 4.0 and 15 Au^{2+}/nm^2.

Defect Diffusion

Figure 1 shows the depth profiles of the Si disorder in SiC irradiated at different temperatures to fluences of 0.1, 0.4, 4.0, and 15 Au^{2+}/nm^2. To compare damage peaks prior to full amorphization, lower fluences were selected for lower irradiation temperatures. The depth shifts of the damage peaks are minimal with the increase of fluence at and below 450 K. The maximum depth shift of the damage peak in this study occurs in the highest-dose sample at

550 K and covers a total distance of ~61 nm from 150 K to 550 K. A fraction of the depth shift (~23 nm) was due to the fluence increase from 4 to 15 Au^{2+}/nm^2 at 550 K, as shown in Figure 1. This shift may be attributed largely to thermal diffusion/migration of Si defects to the bulk. In addition to the defect diffusion, possible substitution of the implanted Au for the Si sublattice may also play a role in enhancing the Si disorder in the Au-rich region. For a fluence of 15 Au^{2+}/nm^2, the maximum atomic fraction of the implanted Au atoms at ~170 nm (Au^{2+} projected range) corresponds to ~14%. From Figure 1(b) and (c), significant dynamic recovery appears to occur between 410 and 450 K for 0.4 Au^{2+}/nm^2 and between 500 and 550 K for 4 Au^{2+}/nm^2.

Dynamic Recovery

Also of interest is dynamic recovery during ion irradiation, because dynamic recovery controls behavior during irradiation. While there have been several investigations of dynamic recovery in 6H-SiC during ion implantation, there have been only a few studies of dynamic annealing on pre-existing damage states in 6H-SiC. Channeling spectra from 0.94 MeV D^+ ions for 6H-SiC irradiated to 200 He^+/nm^2 at 300 K are shown in Figure 2 for the as-damaged state and after additional irradiation near 300 K with 50 MeV I^{10+} to ~0.1 ions/nm^2. The spectra consist of two well-resolved yields from $^{28}Si(d,d)^{28}Si$ RBS/C and $^{12}C(d,p)^{13}C$ NRA/C, which readily allows simultaneous analysis of disorder on both the Si and C sublattices. From Figure 2, there is a significant irradiation-induced recovery of disorder on both the Si and C sublattices between the buried amorphous layer and the surface. In the vicinity of the damage peak, where the disorder level (~0.92) is close to the fully amorphous state, recovery is not observed. Beyond the buried amorphous layer, recovery is again observed, but at a lower rate for both sublattices. These recovery processes lead to a clear sharpening of the damage peak. The results from Figure 2 indicate that the high-energy heavy-ion beam-induced recovery is similar on both the Si and C sublattices in 6H-SiC.

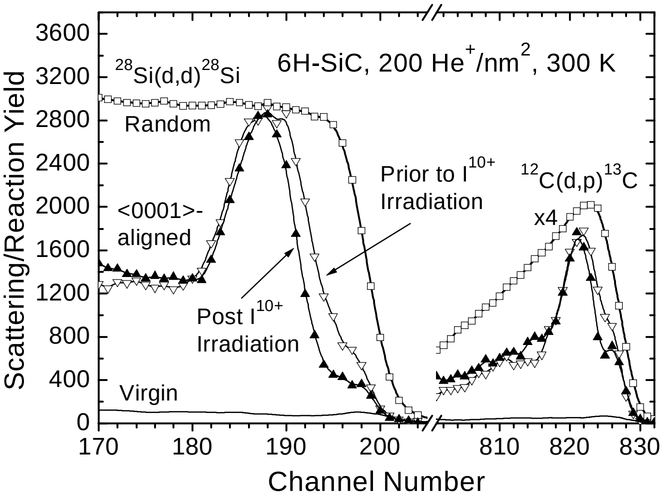

Figure 2. Irradiation-induced recovery of disorder on both the Si and C sublattices in 6H-SiC using 50 MeV I^{10+} ions to a fluence of ~0.1 ions/nm^2 near room temperature.

Irradiation-Induced Recovery in Gallium Nitride

W Jiang[(a)] and W Weber[(a)]

(a) Pacific Northwest National Laboratory, Richland, Washington

Gallium nitride (GaN) possesses a wide bandgap and other outstanding properties that have attracted extensive investigations of ion-implantation effects associated with the fabrication of advanced electronic and optoelectronic devices. One of the biggest challenges at present is the issue associated with the efficient removal of the implantation damage in GaN. Further research is required to explore methods for damage recovery without involving harsh thermal annealing conditions. Recent studies have indicated that a reconstruction of amorphized GaN occurs following light-ion irradiation in GaN.

The depth profiles of the relative disorder on the Ga sublattice in GaN irradiated to 3.8 Au^{2+}/nm^2, followed by thermal annealing at 873 K for 7 and 30 min or Si^{2+} irradiation at 873 K to 5 and 30 Si^{2+}/nm^2, are shown in Figure 1. During thermal annealing, there is considerable recovery of defects in the near-surface region for the first 7 min; however, further annealing (30 min) does not lead to appreciable additional recovery. In the deeper region (>20 nm), the disorder profile is largely unaffected by the thermal annealing process. Because the nature of the damage is different near the surface (point defects and small defect clusters) and in the bulk peak region (planar defects and amorphous domains), the result suggests that the thermal recovery may be associated with a relatively higher concentration of mobile point defects.

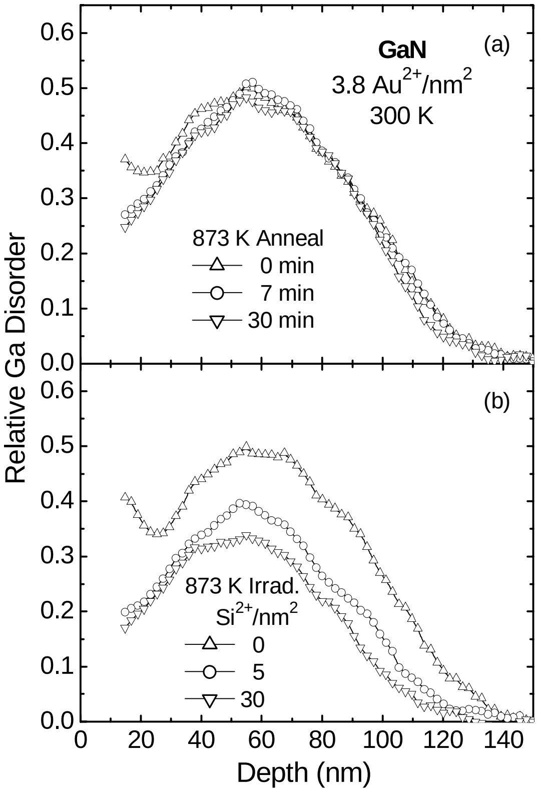

Figure 1. Depth profiles of the relative disorder on the Ga sublattice in GaN irradiated to 3.8 Au^{2+}/nm^2 at 300 K: (a) annealed at 873 K for 7 and 30 min, and (b) irradiated at 873 K with 5.4 MeV Si^{2+} ions to 5 and 30 ions/nm^2.

The results of the Si^{2+} irradiation on Ga damage profiles are shown in Figure 1(b). In contrast to Figure 1(a), significant defect recovery occurs at all depths over the damage profile (15 to 130 nm) during the Si^{2+} irradiation to 5 ions/nm^2. Further recovery of the damage is observed for a larger fluence (30 Si^{2+}/nm^2).

As indicated by a comparison of the results in Figures 1(a) and 2(b), dynamic annealing processes during irradiation can induce disorder recovery in GaN that cannot be attained by thermal processes at 873 K.

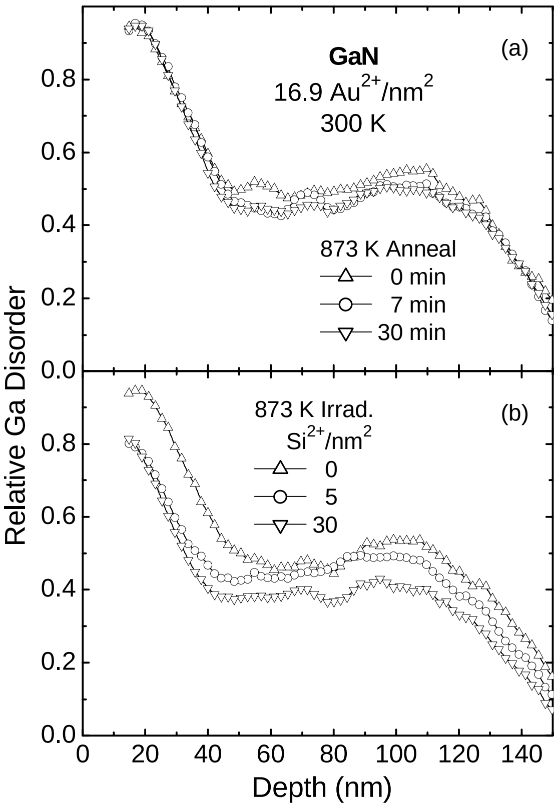

Figure 2. Depth profiles of the relative disorder on the Ga sublattice in GaN irradiated to 16.9 Au^{2+}/nm^2 at 300 K: (a) annealed at 873 K for 7 and 30 min, and (b) irradiated at 873 K with 5.4 MeV Si^{2+} ions to 5 and 30 ions/nm^2.

In a more highly damaged GaN crystal (16.9 Au^{2+}/nm^2), thermal and dynamic behavior of the Ga disorder is shown in Figure 2. In general, no significant recovery of the Ga disorder profile occurs during thermal annealing at 873 K for times up to 30 min. In contrast to the behavior observed at the lower ion fluence in Figure 1(a), the higher level of damage in the surface regime (<50 nm) remains unchanged after the thermal annealing; this finding indicates that the local damage state is more thermally stable than that present at the lower ion fluence, which implies a lower concentration of mobile defects. Only a small reduction in the Ga disorder concentration is observed in the disorder saturation regime (between 50 and 120 nm) for the first 7 min and then remains at the damage level during further annealing at 873 K for 30 min. Within experimental error, this behavior is similar to the recovery behavior observed in this depth regime for the lower fluence specimen shown in Figure 2(a). Recent transmission electron microscopy studies have indicated that this depth region contains a dense network of dislocation loops and highly disordered domains. According to Figure 2(a), most of these defects are thermally stable at 873 K, and there are insufficient point defects to stimulate any measurable recovery. The effect of irradiation with 5.4 eV Si^{2+} ions at 873 K on the recovery is shown in Figure 2(b). During irradiation to 5 ions/nm^2, there is significant recovery of the Ga disorder in the surface region, where the material was rendered nearly completely amorphous at the depth of ~18 nm. As in the case of the lower ion fluence specimen, this irradiation-enhanced recovery is most likely the result of Frenkel pair formation that stimulated recovery of stable defect clusters and/or amorphous domains. Recovery of amorphous domains would most likely be attributed to defect-stimulated epitaxial regrowth at any crystalline-amorphous interfaces. From Figures 2(a) and (b), thermal epitaxial recrystallization apparently does not occur at 873 K without the presence of simultaneous irradiation.

Analysis of Helium Retention in SiC as a Function of Irradiation and Annealing Using Ion Beams

R Smith,[(a)] V Shutthanandan,[(b)] Y Zhang,[(b)] L Bissell,[(c)] S Thevuthasan,[(b)] W Jiang,[(d)] and W Weber[(d)]

(a) Montana State University, Bozeman, Montana
(b) W.R. Wiley Environmental Molecular Sciences Laboratory, Richland, Washington
(c) Brigham Young University, Provo, Utah
(d) Pacific Northwest National Laboratory, Richland, Washington

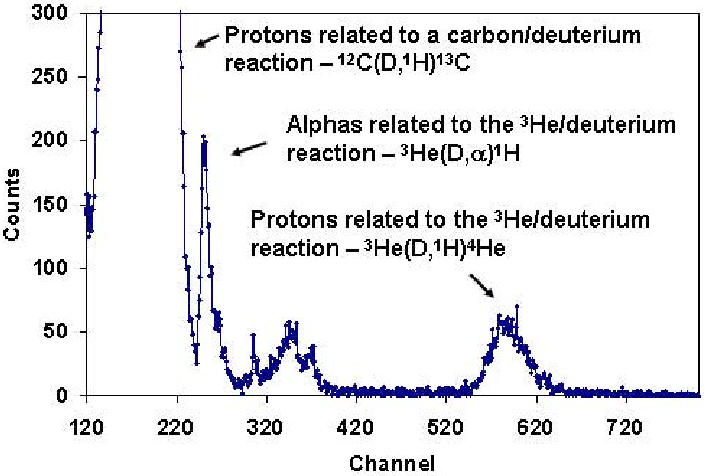

Figure 1. Nuclear reaction products from the ^{3}He-implanted region of the SiC sample.

Silicon carbide (SiC) has been proposed for coating applications in advanced reactor designs, so studies of its behavior in the presence of ion irradiation and fission products are of interest. Retention of helium in single-crystal 6H-SiC was studied as a function of irradiation dose and annealing temperature using both nuclear reaction analysis (NRA) and time-of-flight, elastic-recoil-detection analysis (TOF-ERDA). Ions of $^{3}He^{+}$ were implanted at 40 keV in SiC to a depth of ~360 nm at room temperature. NRA was performed using 1.0 MeV D^{+} and the $^{3}He(D,\alpha)^{1}H$ reaction (Figure 1).

No change in the He profile was seen for the irradiation dose up to 4×10^{18} D^{+}/cm^{2} at room temperature. Isochronal annealing of the SiC between 300 and 1400 K also showed no significant helium loss. Subsequently, a sample was irradiated with D^{+} at 900 K and again at 1100 K. No loss of helium associated with irradiation was seen for the dose up to 1.4×10^{18} D^{+}/cm^{2}. Annealing the sample above 1400 K resulted in thermally activated loss of He. TOF-ERDA measurements were performed using 44 MeV $^{129}I^{10+}$ for both irradiation and analysis. Depth profiles of the He distribution showed no significant change under I bombardment with an ion fluence up to ~1014 cm^{-2} at room temperature. NRA was performed on the implanted sample subjected to TOF-ERDA analysis. The helium profiles for regions subjected to I irradiation were similar in shape to those with no I irradiation.

Characterization of Single-Crystal Oxide Interfaces

C Wang,[(a)] S Thevuthasan,[(a)] V Shutthanandan,[(a)] F Gao,[(b)] D McCready,[(a)]
S Chambers,[(b)] and C Peden[(b)]
(a) W.R. Wiley Environmental Molecular Sciences Laboratory, Richland, Washington
(b) Pacific Northwest National Laboratory, Richland, Washington

CeO_2 films doped with Y, Zr, Gd, Sm or a lanthanide element have been explored for use as oxygen storage components in catalytic converters and ionic conductors in solid oxide fuel cells. The properties of these films are normally controlled by the defects in the film and the interface. Defects in thin films are normally initiated from the interface between the film and the substrate. Therefore, defects and their spatial distribution within a film may be controlled by carefully tailoring the factors that determine the interface structure. Although the interface structure of *c*-CeO_2 film grown on *c*-ZrO_2 has been investigated previously by ion channeling experiments, a study dedicated to direct observation of the interface structure using transmission electron microscopy has not been carried out. We have used high-resolution transmission electron microscopy (HR-TEM) to characterize the interface structure of such a system.

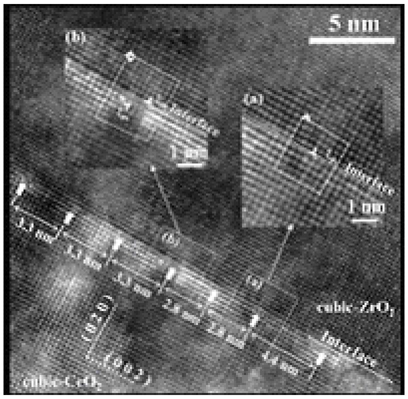

Figure 1. High-resolution transmission electron micrograph of $CeO_2(100)$/ Y-$ZrO_2(100)$.

A cubic-CeO_2 thin film has been epitaxially grown on a yttria-stabilized ZrO_2 substrate by oxygen-plasma-assisted molecular beam epitaxy. Structural features of the interface between the films and the substrates were characterized by Rutherford Backscattering Spectrometry (RBS), x-ray diffraction, and HR-TEM (Figure 1). RBS channeling spectra for both CeO_2/ZrO_2 show interface disorder-related scattering peaks believed to be due to interface misfit dislocations. Cross-sectional HR-TEM reveals that interfaces of both systems are similarly characterized by coherent regions that are separated by misfit dislocations periodically distributed along the interface. The experimentally observed dislocation spacing is approximately consistent with those calculated from the lattice mismatch. Similar misfit dislocations were observed in single-crystal α-$Fe_2O_3(0001)$ grown on α-$Al_2O_3(0001)$ (Wang et al. 2002, 2003).

References

Wang CM, S Thevuthasan, F Gao, DE McCready, and SA Chambers. 2002. "The Characteristics of Interface Misfit Dislocations for Epitaxial α-Fe_2O_3 on α-$Al_2O_3(0001)$." *Thin Solid Films* 414:31-38.

Wang CM, S Thevuthasan, and C Peden. 2003. "Interface Structure of an Epitaxial Cubic Ceria Film on Cubic Zirconia." *Journal of the American Ceramic Society* 86(2):363-365.

Redox Properties of Water on the Oxidized and Reduced Surfaces of $CeO_2(111)$

M Henderson,[a] C Perkins,[a] M Engelhard,[b] S Thevuthasan,[b] and C Peden[a]
(a) Pacific Northwest National Laboratory, Richland, Washington
(b) W.R. Wiley Environmental Molecular Sciences Laboratory, Richland, Washington

Ceria is an oxide with many interesting catalytic properties, with its ability to accommodate variable levels of bulk and surface reduction being one of the more important ones. This characteristic of ceria materials makes it suitable for use as a support for catalytic water on $CeO_2(111)$ applications where the reaction conditions fluctuate between oxidizing and reducing conditions. In many of these applications, water is present as either a reactant (e.g., the water-gas shift reaction) or as a product/spectator (e.g., selective oxidation reactions). Despite the potential importance of the water-ceria interaction, the system has not been studied much. The most notable property in the literature regarding the water-ceria interaction is the observation that water oxidizes Ce^{3+} sites to Ce^{4+}. In this study, we examine the chemistry of water on the oxidized and reduced surfaces of $CeO_2(111)$. Our results suggest that $CeO_2(111)$ thin films on yttria-stabilized $ZrO_2(111)$ [YSZ(111)] are considerably easier to vacuum reduce than is the (111) surface of bulk single crystals. This difference likely results from the >104 greater capacity of a millimeter-thick single-crystal sample to act as a bulk "reservoir" for oxygen vacancies compared to the capacity of the 500-Å film used here. Our results with water suggest that Ce^{3+} sites on the reduced (111) surface are resistant to oxidation by water under ultra-high vacuum (UHV) conditions and that high-temperature treatment with water may instead promote further reduction of the surface. A portion of this work is briefly described below.

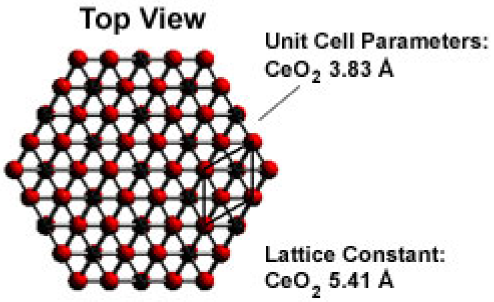

Figure 1. Surface structure of $CeO_2(111)$.

This summary describes the x-ray photoelectron spectroscopy (XPS) and temperature-programmed desorption (TPD) results from probing the surface chemistry of water on the oxidized and reduced surfaces of a 500-Å epitaxial $CeO_2(111)$ film grown on YSZ(111) (Figure 1). Results show that epitaxial films of $CeO_2(111)$ on YSZ(111) are readily reduced by annealing under UHV conditions at temperatures between 773 and 973 K (Henderson et al. 2003). XPS analysis indicates that the majority of reduction is located in the outer layer of the $CeO_2(111)$ film, with levels of surface reduction reflective of a suboxide of ceria achieved by annealing above 840 K. TPD and XPS studies indicate that water does not oxidize Ce^{3+} sites on the reduced $CeO_2(111)$ surface under UHV conditions below 650 K. In fact, XPS results suggest that water exposure at 650 K increases the level of $CeO_2(111)$ surface reduction, presumably by stabilizing Ce^{3+} sites at the surface that result from bulk-to-surface diffusion of oxygen vacancies. The reactivity of Ce^{3+} surface sites toward water likely depends on the surface termination and morphology. In particular, while water was unable to oxidize Ce^{3+} sites on atomically flat $CeO_{2-x}(111)$ surfaces, water has been observed to oxidize Ce^{3+} sites on reduced CeO_2 powders and lattice mismatched films of

CeO_{2-x}(111) on Ru(0001). In general, this finding implies that the diverse surfaces of crystalline nanoparticles of ceria may simultaneously support oxidation and reduction reactions of the same molecule on different parts of the particle, with the flow of electronic defects between different surfaces on the same particle potentially promoting resurfacing of the particle.

Reference

Henderson MA, CL Perkins, MH Engelhard, S Thevuthasan, and CHF Peden. 2003. "Redox Properties of Water on the Oxidized and Reduced Surfaces of Ceo_2 (111). *Surface Science* 526:1-18.

Damage Accumulation and Recovery in $Cd_2Nb_2O_7$

W Jiang,[(a)] *W Weber,*[(a)] *S Thevuthasan,*[(b)] *and L Boatner*[(c)]
(a) Pacific Northwest National Laboratory, Richland, Washington
(b) W.R. Wiley Environmental Molecular Sciences Laboratory, Richland, Washington
(c) Oak Ridge National Laboratory, Oak Ridge, Tennessee

Pyrochlores are typically ternary oxides that crystallize into a cubic structure with the general chemical formula $A_2B_2O_7$, where elements A and B are trivalent (or divalent) and tetravalent (or pentavalent) cations, respectively. Elemental versatility in the crystal structure ensures that pyrochlore compounds exhibit a variety of interesting properties, including ionic conduction, catalytic activity, and fluorescence. In addition, rare-earth titanate and zirconate pyrochlores are recognized as having a great potential for immobilization and permanent disposal of high-level radioactive nuclear wastes due to possible substitutions of radionuclide species, such as actinide elements, for cation A. This study addresses the damage accumulation in Au^{2+}-irradiated $Cd_2Nb_2O_7$ at 150 K and 300 K and room-temperature recovery of defects in $Cd_2Nb_2O_7$ (Jiang et al. 2003).

Damage Accumulation

The dependence of the relative Cd and Nb disorder (at the damage peak) on dose (dpa) and ion fluence (Au^{2+}/nm^2) is shown in Figure 1 for Au^{2+} irradiations at 150 and 300 K, where full amorphization corresponds to a value of unity (1.0) on the vertical scale. The crystal used for irradiation at 150 K had a high crystalline quality; however, there is a measurable pre-existing defect concentration in the specimen used for 300 K irradiation in this study, and the relative disorder on both the Cd and Nb sublattices in the near-surface regime has been estimated to be ~0.1. To compare the disordering behavior of $Cd_2Nb_2O_7$ at 150 and 300 K an empirical method was used to subtract the offset of the relative disorder based on the expression $[S(D)-S(0)]/[1-S(0)]$, where S (D) is the as-measured relative disorder at dose D, and $S(0)$ is the pre-existing relative disorder at $D=0$. This method normalizes the measured relative disorder in such a way that the corrected relative disorder is set to 0 at zero dose and to 1 at the amorphization dose. The corrected data are also plotted in Figure 1 as a function of dose for the purpose of comparison.

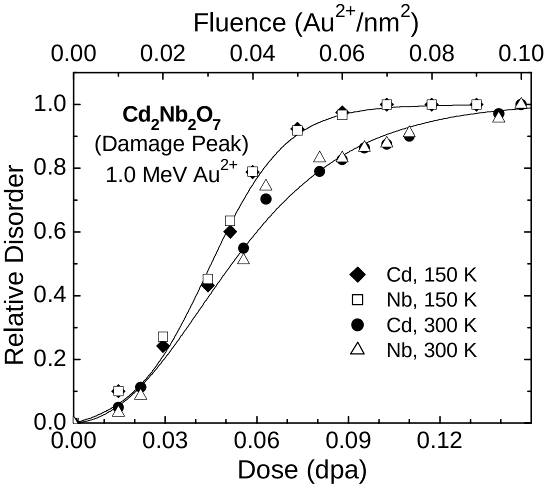

Figure 1. Relative disorder on the Cd and Nb sublattices as a function of dose at the damage peak in $Cd_2Nb_2O_7$ irradiated at 150 and 300 K with 1.0 MeV Au^{2+} ions. The solid lines are sigmoidal fits to the data for both sublattices.

Results in Figure 1 show that the disordering rate on the Cd and Nb sublattices at each individual dose is nearly the same at both 150 and 300 K, which is consistent with the prediction by the SRIM-97 software. The solid lines in Figure 1 are generic sigmoidal fits to the Cd and Nb data at 150 and 300 K, which are generally consistent with the direct-impact, defect-stimulated model for amorphization. From Figure 1, there is a general dose shift to a higher value for irradiation at 300 K compared to irradiation at 150 K. This behavior is primarily associated with the dynamic recovery processes during Au^{2+} irradiation at 300 K. The amorphization dose increases from 0.10 dpa at 150 K to 0.15 dpa at 300 K. The amorphization dose for Cd_2Nb_2O7 irradiated with Ne^+ and Xe^{2+} at room temperature were previously shown to be 0.65 and 0.22 dpa, respectively, where the same threshold displacement energy (E_d = 25 eV for each sublattice) as we assumed in this study was adopted in that SRIM-97 simulation. These results indicate a systematic decrease in the amorphization dose at room temperature with increasing ion mass (damage energy density).

Room-Temperature Recovery

Figure 2 shows the recovered fraction of defects at the damage peak in $Cd_2Nb_2O_7$ irradiated at 150 and 300 K during thermal annealing at room temperature for 38 hours. There is considerable recovery of the defects, produced at 150 K, for damage levels between 0.6 and 0.97. The recovery fraction appears to decrease with the increase of relative disorder, ranging from 20% at relative disorder of 0.6 to 10% at 0.97; it vanishes at 1.0, indicating that recrystallization of the fully amorphized $Cd_2Nb_2O_7$ did not occur at room temperature. It is expected, however, that there is a certain degree of room-temperature recovery at the low doses. In contrast to the significant recovery of the defects produced at 150 K, there is negligible room-temperature recovery of the defects produced at 300 K over the damage levels from 0.2 to 1.0, as shown in Figure 2. This result indicates that these defects are stable at room temperature.

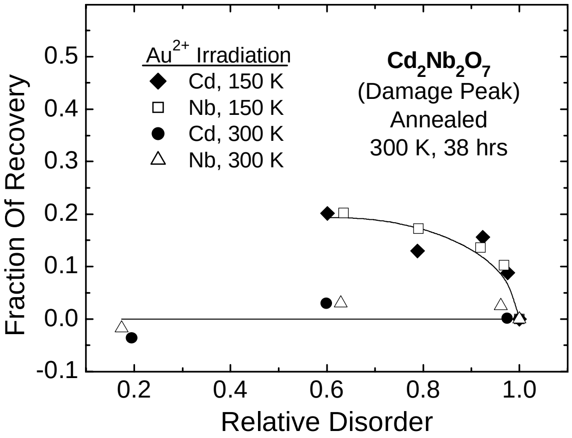

Figure 2. Room-temperature recovery (38 hours) of defects at the damage peak in $Cd_2Nb_2O_7$ irradiated at 150 and 300 K with 1.0 MeV Au^{2+} ions.

Reference

Jiang W WJ Weber, S Thevuthasan, and LA Boatner. 2003. "Effect of Ion Irradiation in Cadmium Niobate Pyrochlores." *Nuclear Instruments and Methods in Physics Research B* 207:85-91.

Ion-Beam-Synthesized, Room-Temperature-Diluted Magnetic Semiconductor: Co-Implanted Rutile TiO_2(110) Single Crystal

V Shutthanandan,[a] S Thevuthasan,[a] S Heald,[b] T Droubay,[b] M Engelhard,[a] T Kaspar,[b] D McCready,[a] L Saraf,[a] S Chambers,[b] B Mun,[c] N Hamdan,[c] P Nachimuthu,[c] B Taylor,[e] R Sears,[d] and B Sinkovic[d]

(a) W.R. Wiley Environmental Molecular Science Laboratory, Richland, Washington
(b) Pacific Northwest National Laboratory, Richland, Washington
(c) Advanced Light Source, Lawrence Berkeley National Laboratory, Berkeley, California
(d) University of Connecticut, Storrs, Connecticut

There is a growing interest in diluted magnetic semiconductors (DMS) for the emerging field of spintronics. For example, the ability to efficiently inject spin-polarized carriers into non-magnetic semiconductor heterostructures creates new and exciting possibilities for utilizing DMS materials in spin-based devices. Several III-V and II-VI semiconductor materials doped with magnetic transition elements have been explored as candidates for DMS applications. Although these materials show promising behavior, they exhibit Curie temperatures of ~170 K or less. It has recently been demonstrated that certain oxide semiconductors doped with magnetic transition elements show room-temperature ferromagnetism. Titanium dioxide in both anatase and rutile phases appears to be among the most promising oxide semiconductors for DMS applications. Unlike conventional semiconductors, these materials exhibit Curie temperatures of at least 400 K, making them the most magnetically robust oxide semiconductors discovered to date. We report the results from $5.0x10^{16}$ Co^+/cm^2 implanted rutile TiO_2(110).

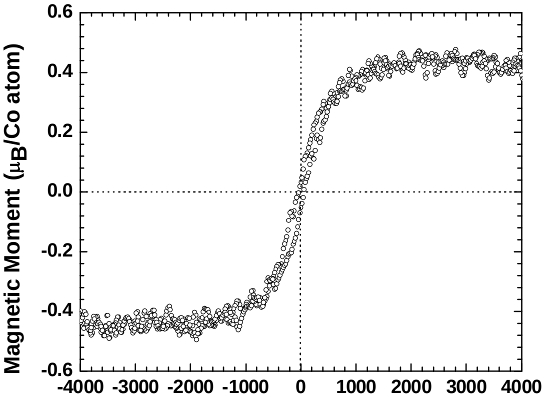

Figure 1. VSM hysteresis loop for ~2 at. % Co-implanted TiO_2 (110) rutite.

A typical hysteresis loop taken from the Co-implanted TiO_2(110) rutile sample at room temperature with a Lakeshore 7300 vibrating sample magnetometer (VSM) is shown in Figure 1. The magnetic field was oriented perpendicular to the sample surface during this experiment. However, there were no noticeable differences between in-plane or perpendicular magnetization loops. The sample clearly shows ferromagnetic behavior with a saturation magnetization of ~0.4 μ_B/Co atom, assuming that all the Co atoms contribute to the magnetization. This value is less than that of pure Co metal (1.7 μ_B/Co atom) and that found for Co-doped TiO_2 anatase grown by molecular beam epitaxy (~1.2 μ_B/Co atom) but comparable to Co-doped rutile TiO_2 films (0.3 to 0.6 μ_B/Co atom) grown by other techniques. The coercive field was found to be ~100 Oe with a remanence of ~20%.

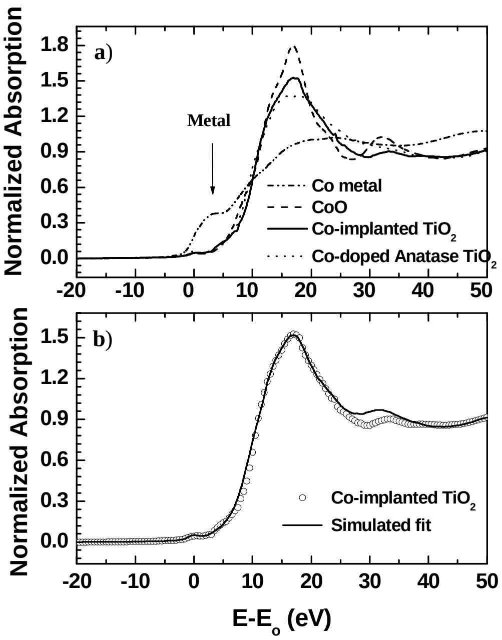

Figure 2. (a) Co K-edge XANES spectra from Co metal, CoO, $CoTiO_3$, and Co-implanted rutile TiO_2. (b) Co K-edge XANES spectra (open circles) along with simulation consisting of a weighted average (solid line) of Co spectra from various reference materials.

We used Co L-edge and K-edge x-ray absorption near-edge structure (XANES) to obtain the charge state of Co in TiO_2. Co K-edge XANES spectra from Co-implanted rutile TiO_2 and various Co-containing reference materials (Co metal, CoO, and Co-doped anatase) are shown in Figure 2(a). The spectral feature at $E-E_o$= 2-3 eV is unique to Co metal and can be effectively used, along with the large chemical shift associated with oxidized Co, to investigate the presence of Co metal. This feature is different from the small feature observed at $E-E_o$= 0 eV, which is caused by a 1*s* to 3*d* pre-edge resonance that becomes dipole allowed when Co is non-octahedrally coordinated to O ligands. Hence, it is clear that the low-energy feature associated with Co(O) is absent in spectra for Co implanted TiO_2, as well as in spectra for oxidized Co (Co-doped anatase and CoO). Thus, there is no detectable Co(O) present in Co-implanted TiO_2 rutile. We have carried out a weighted fitting procedure to fit the experimental K-edge XAS data. In this fitting procedure, the weighted averages of Co (metal), CoO, and Co-doped anatase spectra were used to fit the experimental data. The result obtained from this fitting procedure is shown in Figure 2(b). The best fit is obtained for 0% Co, 64% Co-doped anatase, and 36% CoO. Hence, Co is in the +2 formal oxidation states in the sample, and the local structural environment, to which XANES is highly sensitive, can be represented by an admixture of Co-doped anatase and CoO reference spectra. Based on the presence of a CoO peak in the x-ray diffraction scan and the 36% CoO weighting factor in the Co K-edge XANES simulation, it is highly likely that some of the implanted Co is present as a CoO secondary phase. Because CoO is antiferromagnetic, the total saturation magnetization of 0.4 μ_B/Co atom is a lower limit in that some fraction of the Co (that in CoO) is not contributing to the ferromagnetic response.

Growth of Cr-doped TiO_2 Films in the Rutile and Anatase Structure by Oxygen-Plasma-Assisted Molecular Beam Epitaxy

J Osterwalder,(a) *T Droubay,*(b) *T Kaspar,*(b) *J Williams,*(b) *and S Chambers*(b)
(a) Physik-Institut, Universität Zürich, Switzerland
(b) Pacific Northwest National Laboratory, Richland, Washington

As part of a search for new spintronic materials, and encouraged by recent successes in the $Co_xTi_{1-x}O_2$ anatase system, highly ordered films of $Cr_xTi_{1-x}O_2$ in both the rutile and anatase structure and for several Cr concentrations ranging from x=0.02 to 0.13 were grown by oxygen-plasma-assisted molecular beam epitaxy. Chromium has been found to be a suitable dopant for several IV, III-V, and II-VI semiconductors, producing diluted magnetic semiconductor (DMS) materials with ferromagnetic Curie temperatures reaching or exceeding room temperature in several cases.

Reflection high-energy electron diffraction (RHEED) and atomic force microscopy (AFM) measurements show that rutile films grown on $TiO_2(110)$ rutile substrates are extremely flat, while the anatase films grown on $LaAlO_3(001)$ substrates are fairly rough. From a careful analysis of the RHEED intensity oscillations during growth, before and after opening the Cr shutter (Figure 1), a precise calibration of the Cr concentration of this particular film, as well as its thickness could be obtained. The inset in the figure shows the deposition times where the oscillation maxima occur, measured from some offset time before or at the time of the Cr shutter opening. Linear regression to these data points leads to oscillation periods T_{osc} of 44.1(3) s and 39.3(4) s, respectively. The additional flux from the Cr source accounts for the faster film growth and, thus, the shorter oscillation period. This observation indicates a uniform distribution of Cr throughout the film, at least for this initial stage of the growth. Cr concentrations for other films were obtained from x-ray photoelectron spectroscopy core-level intensity ratios, using this reference film for absolute calibration.

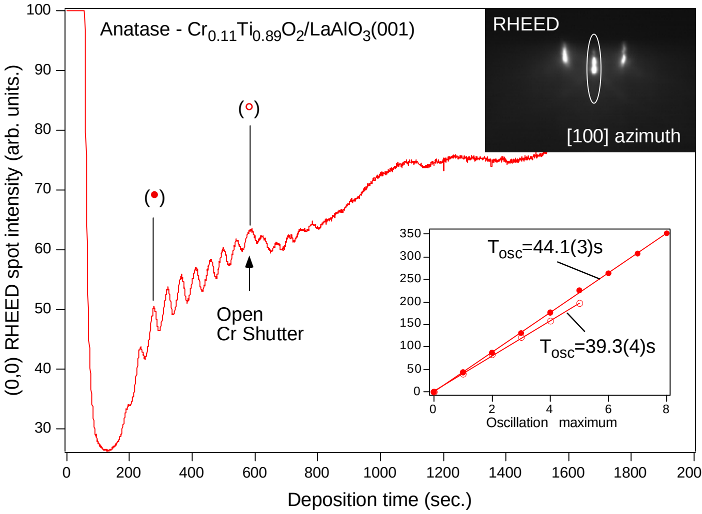

Figure 1. Intensity of the specular RHEED spot during the growth of a $Cr_{0.11}Ti_{0.89}O_2$ anatase film on $LaAlO_3(001)$ as a function of deposition time. The inset in the upper right corner shows the substrate RHEED pattern at the outset of the film growth. The inset in the bottom right corner displays the positions of intensity oscillation maxima before (filled circles) and after (open circles) opening the Cr shutter.

For both rutile and anatase films, x-ray photoelectron diffraction data of the Cr 2p level (Figure 2), taken *in situ* but after completion of the film growth, exhibit the same patterns and the same modulation amplitudes as those observed for Ti 2p, providing a strong indication that a large fraction of the Cr atoms occupy substitutional lattice sites in both structures.

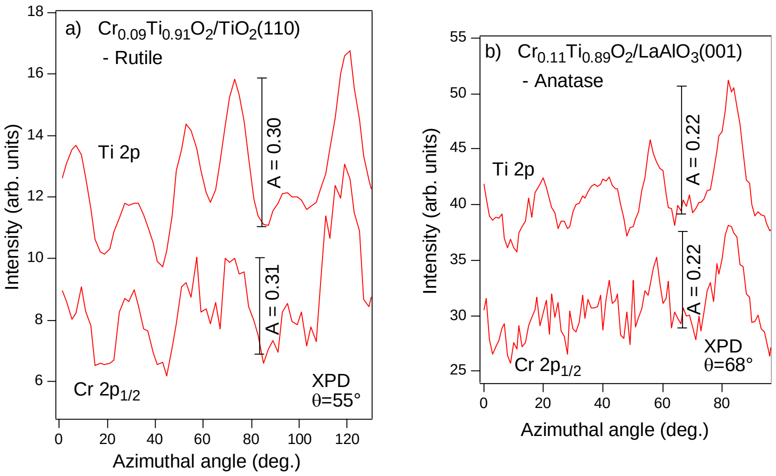

Figure 2. (a) X-ray photoelectron diffraction azimuthal scan of Ti 2p and Cr $2p_{1/2}$ emission from a $Cr_{0.09}Ti_{0.91}O_2$ rutile film. (b) Same, but from a $Cr_{0.11}Ti_{0.89}O_2$ anatase film. The absolute anisotropies, A, of a prominent feature are indicated for all curves.

Three different spectroscopic investigations addressing the question of the charge state of the Cr ions were carried out. The Cr 2p spectra, a Cr 3d-related dopant signal above the valence band of TiO_2 (see Figure 3), and the Cr K-shell x-ray absorption spectrum are characteristic of Cr^{3+} ions. The Cr 3d states appear at slightly different binding energies for the two structures: 2.6(1) eV for rutile and 2.2(1) eV for anatase. For rutile, this brings the Cr 3d level to a position of 0.3 eV above the top of the valence band.

Preliminary vibrating sample magnetometer measurements at room temperature on the $Cr_{0.11}Ti_{0.89}O_2$ anatase film produced a clear ferromagnetic signal, with about half a Bohr magneton saturation moment per Cr ion, and a coercivity of 110 gauss. Further experiments for confirming these promising results are underway before Cr-doped anatase films can be announced as a new dilute DMS.

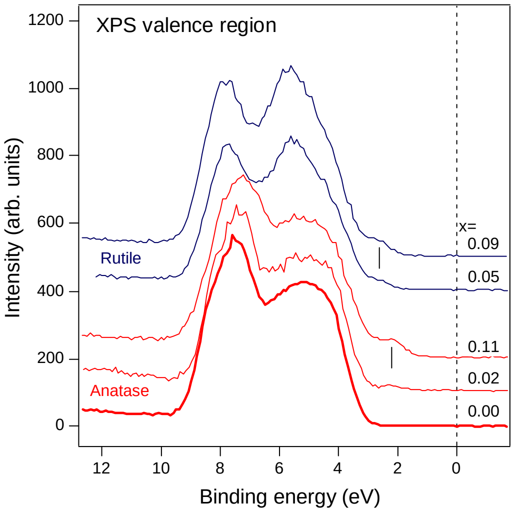

Figure 3. Monochromatized Al Kα excited x-ray photoelectron spectroscopy valence spectra for $Cr_xTi_{1-x}O_2$ anatase (bottom three curves) and rutile (top two curves) films for varying Cr concentration x. Vertical marks indicate the positions of Cr 3d states.

Damage Accumulation and Amorphization in Samarium Titanate Pyrochlore

Y Zhang,[(a)] *V Shutthanandan,*[(a)] *R Devanathan,*[(b)] *S Thevuthasan,*[(a)] *D McCready,*[(a)] *J Young,*[(a)] *and W Weber*[(b)]
(a) W.R. Wiley Environmental Molecular Sciences Laboratory, Richland, Washington
(b) Pacific Northwest National Laboratory, Richland, Washington

Materials of composition $A_2B_2O_7$ with the pyrochlore structure have remarkable elemental versatility, which makes these materials of considerable interest for the immobilization of actinide-rich nuclear waste. As a result of alpha decay, actinide-bearing phases will be subjected to considerable self-radiation damage. Radiation damage from alpha decay can result in amorphization, macroscopic swelling, and order-of-magnitude increases in dissolution rates; these structural changes significantly affect the long-term performance of nuclear waste forms.

Irradiation with gold ions was recently used to simulate alpha-recoil damage in samarium titanate pyrochlore ($Sm_2Ti_2O_7$) single crystals (Zhang et al. 2004) using the 3.0-MV tandem accelerator facility in the W. R. Wiley Environmental Molecular Sciences Laboratory. The irradiation-induced defects are, for the first time, quantitatively characterized by channeling Rutherford backscattering spectrometry to achieve a better understanding of damage accumulation processes, which is essential to predicting long-term performance of $A_2B_2O_7$ pyrochlores used to immobilize the actinides.

Damage accumulation under 1.0-MeV Au^{2+} irradiation at 170, 300, and 700 K is shown in Figure 1. The results indicate that the atomic disorder increases nonlinearly with dose, which is described well by a disorder accumulation model. Based on the fit to the disorder accumulation model, defect-stimulated amorphization is a primary mechanism leading to amorphization in $Sm_2Ti_2O_7$.

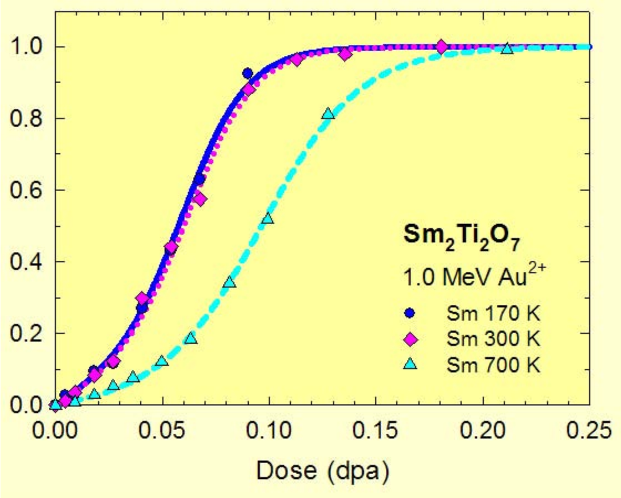

Figure 1. Relative samarium disorder at the damage peak as a function of dose for $Sm_2Ti_2O_7$ irradiated by 1.0-MeV Au^{2+} at 170, 300, and 700 K.

The critical dose for amorphization in $Sm_2Ti_2O_7$ under 0.6-MeV Bi^+ irradiation was studied by *in situ* transmission electron microscopy (TEM) over a temperature range of 30 to 950 K. The selected area electron diffraction (SAED) patterns obtained from samples irradiated at 950 K are shown in Figure 2, which is representative of the general amorphization behavior observed at lower temperature irradiations. With increasing dose, the intense diffraction spots begin to fade, and amorphous halos appear in the SAED patterns. The pyrochlore

Figure 2. Diffraction patterns of $Sm_2Ti_2O_7$ irradiated with 0.6-MeV Bi^+ at 950 K. (a) Original, (b) 0.34 dpa, and (c) 0.61 dpa.

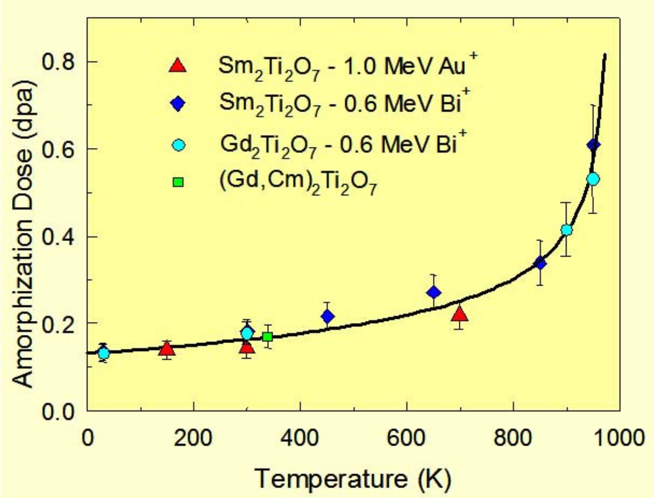

Figure 3. Critical dose for amorphization of $Sm_2Ti_2O_7$ and $Gd_2Ti_2O_7$ irradiated by 1.0-MeV Au^{2+}, and 0.6-MeV Bi^+. Also included are results for amorphization in $Gd_2Ti_2O_7$ doped with 3 wt% ^{244}Cm.

crystal structure, as shown by the diffraction pattern, gradually amorphizes, all the diffraction spots vanish, and only the amorphous halos remain.

The critical dose for amorphization in $Sm_2Ti_2O_7$ under irradiation with 1.0-MeV Au^{2+} and 0.6-MeV Bi^+ is shown in Figure 3 as a function of temperature. Also included are the TEM results for $Gd_2Ti_2O_7$ irradiated with 0.6-MeV Bi^+ and due to alpha decay. Despite the six orders of magnitude difference in damage rates, the good agreement between the amorphization doses in $Sm_2Ti_2O_7$ and $Gd_2Ti_2O_7$ under heavy ion irradiation and in $Gd_2Ti_2O_7$ due to ^{244}Cm decay indicate that amorphization due to heavy-ion energy deposition is relatively independent of dose rate at about room temperature. As a result, the model of damage accumulation and amorphization under heavy-ion irradiation in rare-earth titanates can be used to assess the impact of alpha-decay events on long-term performance.

Reference

Zhang Y, WJ Weber, V Shutthanandan, R Devanothan, S Thevuthasan, C Balakrishnan, and DM Paul. 2004. "Damage Evolution on Sm and O Sublattices in Au-Implanted Samonium Titanate Phyrochlore." *Journal of Applied Physics* 95:28-72.

Growth and Properties of MBE Grown Ferromagnetic Fe-Doped TiO_2 Rutile Films on TiO_2(110)

Y Kim,[(a)] S Thevuthasan,[(b)] T Droubay,[(c)] A Lea,[(b)] C Wang,[(b)] V Shutthanandan,[(b)] S Chambers,[(c)] R Sears,[(d)] B Taylor,[(d)] and B Sinkovic[(d)]
(a) Hanbat National University, Korea
(b) W.R. Wiley Environmental Molecular Sciences Laboratory, Richland, Washington
(c) Pacific Northwest National Laboratory, Richland, Washington
(d) University of Connecticut, Storrs, Connecticut

There is growing interest in thermally robust diluted magnetic semiconductors (DMS) for a number of device concepts in spintronics. Although a number of materials have been investigated, III-V and II-VI semiconductors doped with magnetic transition elements have received the most attention in the past. Oxide semiconductors doped with magnetic transition elements are another promising class of materials. In particular, titanium dioxide appears to be the most promising candidate in terms of exhibiting a high Curie temperature. Building on our experience in the growth and characterization of Co-doped TiO_2 anatase by oxygen-plasma assisted molecular beam epitaxy (OPA-MBE), we have investigated the growth of Fe-doped TiO_2 on rutile TiO_2(110) substrates.

The atomic force microscopy (AFM) and scanning-electron-microscopy (SEM) images obtained in a self-assembled monolayer for x = 0.07 reveal the presence of tall islands on an otherwise flat film surface. A typical SEM image is shown in Figure 1. Isolated clusters of various sizes are clearly visible. Flat and island areas were selected from this image for compositional analysis by SAM. The SAM analyses show that the clusters are Ti-poor and Fe-rich while no measurable amount of Fe is found in the flat areas of the film.

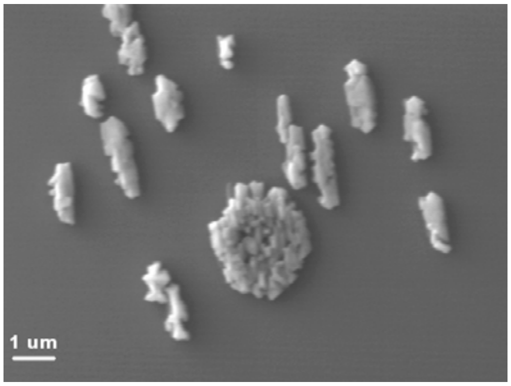

Figure 1. Secondary electron micrograph of a 7% Fe-doped film surface. The lateral dimensions are ~115 x 86 nm.

Magneto-optical Kerr effect (MOKE) and x-ray magnetic circular dichroism (XMCD) measurements are presented in Figures 2 and 3, respectively, for an x = 0.07 film. Magnetic hysteresis loops recorded both perpendicular (polar MOKE) and parallel (longitudinal MOKE) to the sample surface at 300 K show clear ferromagnetic behavior at room temperature. The comparison of the two loops also indicates the easy axis to be in-plane with the remanent magnetization of ~80% and a coercivity slightly greater than 1000 Oe. Additional longitudinal MOKE

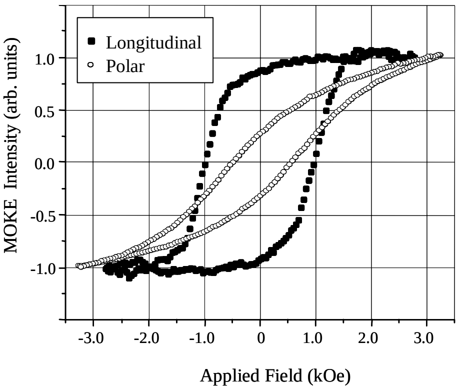

Figure 2. MOKE measurements recorded in longitudinal (in-plane) and polar (out-of-plane) geometry.

measurements with magnetization direction along different in-plane azimuths show no significant changes in their hysteresis loops.

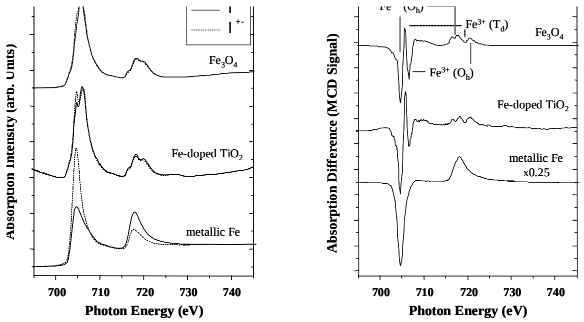

Figure 3. (a) Fe L-edge NEXAFS data collected using right and left circularly polarized light from an Fe_3O_4(001) epitaxial film, a 7% Fe-doped TiO_2 epitaxial film, and Fe metal. (b) The XMCD signal derived from these spectra.

To determine the charge state of Fe in the film, Fe L-edge near-edge x-ray absorption fine structure (NEXAFS) curves were collected using total electron yield detection. The samples were magnetized *in situ*, and measurements were performed in the remanent magnetization state by switching the helicity of the circularly polarized light produced by the elliptically polarized undulator of the beamline BL4.0.2 at the Advanced Light Source (ALS). NEXAFS curves collected with two light polarizations from a well-ordered, single-crystal magnetite Fe_3O_4(001) film, a 7% Fe-doped TiO_2 film, and Fe metal are shown in Figure 3(a).

The XMCD is presented in Figure 3(b) as difference spectra collected with the two x-ray polarizations for the three solids. The XMCD spectra are shown on the same scale except for the metallic Fe, as indicated. Contributions from different Fe-ion sites of ferrimagnetic Fe_3O_4 are also indicated; the Fe^{2+} ions in the octahedral sites (spin-up) and Fe^{3+} ions from the tetrahedral (spin-down) and octahedral sites (spin-up) are consistent with previous reports. Figure 3(b) clearly shows that the XMCD spectrum from the 7% Fe-doped TiO_2 film is very similar to the one from the single-crystal magnetite film in that all the spectral features are seen. However, we note that the line-shape from the 7% Fe-doped TiO_2 film appears to exhibit a slight increase in the population of Fe^{2+} octahedral and Fe^{3+} tetrahedral sites with respect to the Fe^{3+} octahedral sites as compared to the magnetite spectrum. Another possible explanation is that this difference is due to particle-size effects such as reduced coordination at the surface or different crystal field values. Figure 3(b) also shows that the dichroism from the 7% Fe-doped TiO_2 film is very different from that of iron metal. It thus can be concluded that the ferromagnetic properties of the films seen from MOKE and XMCD measurements are due to the presence of pure crystalline inverse spinel Fe_3O_4 particles.

Investigation of Exchange Bias in MnPd/Fe Bilayers

P Blomqvist,[(a)] *X Ji,*[(a)] *K Krishnan,*[(a)] *and D McCready*[(b)]
(a) University of Washington, Seattle, Washington
(b) W.R. Wiley Environmental Molecular Sciences Laboratory, Richland, Washington

The magnetic exchange coupling in nanoscale MnPd/Fe(Co) heterostructures was studied to gain a fundamental understanding of the relationship between structure and magnetic properties in structures that have a strong impact on a variety of technologies. All the samples in this study have been deposited in ultra-high vacuum on single-crystalline MgO (001) substrates using the ion-beam sputtering technique. MnPd and Fe can be grown epitaxially on top of each other, yielding bilayer structures with high crystalline quality. The structural and magnetic properties of the samples were investigated using a combination of techniques available at the W.R. Wiley Environmental Molecular Sciences Laboratory and the University of Washington, including x-ray diffraction (XRD), transmission electron microscopy, Rutherford backscattering, vibrating sample magnetometry, magnetic torque magnetometry, and spin-polarized neutron reflectivity. A very thorough XRD investigation shows MnPd/Fe bilayers with high crystalline quality and well-defined interfaces.

The magnetization measurements show systematic variations in exchange bias behavior as a function of crystallography. This data has been successfully interpreted using a very simple analytical model. As an example of the measurements conducted in EMSL, Figure 1 shows a high-angle XRD scan from a sample deposited at 375°C, which was found to be the optimum growth temperature. At higher temperatures, inter-diffusion between the MnPd and the Fe layer is initiated. As seen in the figure, only the Fe (002) Bragg peak at 65.25° is detected, which indicates that the Fe film is single-crystalline. This finding was verified by an XRD texture scan that showed four (220) reflections with a fourfold symmetry as expected for a body-centered cubic unit cell (Figure 2).

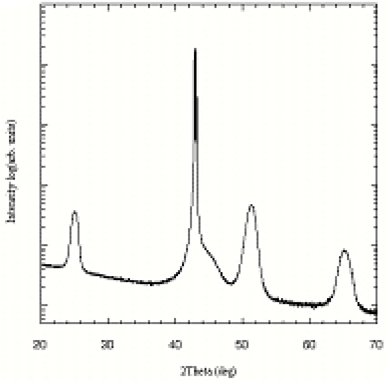

Figure 1. A 2Theta-Omega scan.

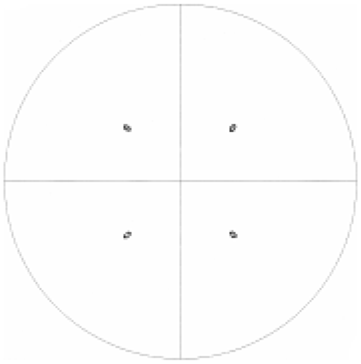

Figure 2. Fe (220) pole figure.

Temperature-Induced Phase Separation in Chromium Films

L Saraf,[a] C Wang,[a] M Engelhard,[a] and D Baer[b]
(a) W.R. Wiley Environmental Molecular Sciences Laboratory, Richland, Washington
(b) Pacific Northwest National Laboratory, Richland, Washington

Chromium metal is known to change its phase upon size reduction. In this study, the possibility of controlled phase separation in chromium was obtained using the knowledge that nanophase chromium exists in a δ-A15 type structure apart from a recently observed fcc phase. The δ-A15 structure is stable up to temperatures ranging from 428°C to 450°C, where significant grain growth and phase transformation to the bcc structure occur. Also, nanophase chromium suppresses the nonmagnetic antiferromagnetic phase transition and gives rise to a surface ferromagnetic phase. Thus, selective phase transformation or controlled phase separation in chromium can be useful for technological applications due to the changed physical properties as a result of different electronic structures with the same base material.

In this study (Saraf et al. 2003), films were deposited with rapid evaporation of chromium and characterized using high-resolution transmission electron microscopy (HR-TEM), atomic force microscopy, and x-ray diffraction (XRD). Vacuum evaporations of chromium on Si(100) were carried out at $3x10^{-5}$ Pa at source-to-sample (SS) distances of 2 cm and 32 cm. The evaporation rate was maintained at ~3 μm/min, which is the fastest rate possible for this system. The tungsten filament of the evaporator also served as the heating source. During evaporation, no additional heating was provided to the substrate. *In situ* thickness measurements were done using a quartz crystal thickness monitor. The thicknesses of the films grown at SS distances of 2 cm and 32 cm were measured as 800 nm and 20 nm, respectively. The samples were exposed to atmospheric pressure 15 min after closing the filament current to ensure that the source filament caused no additional sample heating, especially for the short-distance depositions.

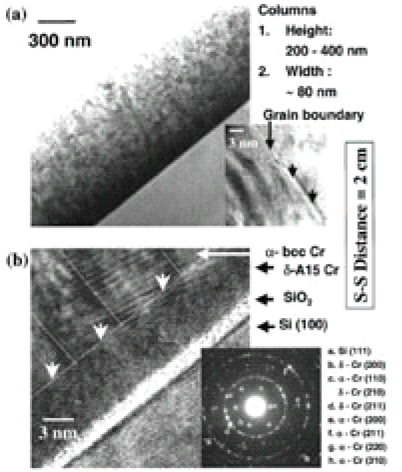

Figure 1. Cross-sectional TEM micrographs of chromium film deposited at a SS distance of 2 cm. (a) Low magnification image across the interface. (Inset: high-resolution cross section of a grain boundary region near the surface.) (b) High-resolution cross section across the interface indicating phase separation. (Inset: electron diffraction pattern.)

A cross-section TEM micrograph of chromium film deposited at a SS distance of 2 cm is shown in Figure 1(a). A columnar-type α structure is observed in the topmost part of the film. Growth of these columns is observed perpendicular to the substrate with the height ranging from 200 nm to 400 nm and an average width of 80 nm. To verify the compactness of these grains, the density variation in the region between the columns was analyzed using HR-TEM of a grain boundary region, as seen as an inset of Figure 1(a). No significant density variation is observed. HR-TEM across the interface of chromium and silicon in the film deposited at a SS distance of 2 cm is shown in Figure 1(b). A 70-Å-thick layer of chromium nanograins is observed near the interface with a very sharp interface between Si and SiO_2. Markers in Figure 1(b) show approximate vertical grain separations and a nanophase layer. Existence of a δ-A15 phase of chromium was verified by a cross-section electron diffraction pattern [Figure 1(b) inset]. Bright reflection circles corresponding to reflections in α-bcc chromium, such as (110), (200), (211), and (220), are clearly visible. Reflections denoted by b, c, and d correspond to (200), (210), and (211) of the δ-A15 phase of chromium.

Structural properties of films grown at SS distances of 2 cm and 32 cm were analyzed by XRD. Scans in the strongest hkl reflection 2θ regions of Cr α-bcc and δ-A15 phases are represented in Figure 2. The chromium α-bcc (110) reflection is observed at 44.6° for growth at a SS distance of 2 cm (Figure 2a). The peak fitting profile indicates the presence of a weak peak of the d-A15 phase at 44.3°. The complete XRD scan of the film deposited at a SS distance of 2 cm is shown as an inset in Figure 2(a). The film deposited at a SS distance of 32 cm [Figure 2(b)] shows a strong (210) reflection at 44.3° attributed to the δ-A15 phase with Cr-O (400) reflection. Dotted lines in Figure 2(b) represent the distinct nature of α and δ-A15 reflections. From the peak broadening in the case of growth at 32 cm, the average grain size is estimated to be ~7 nm at and below 7 nm.

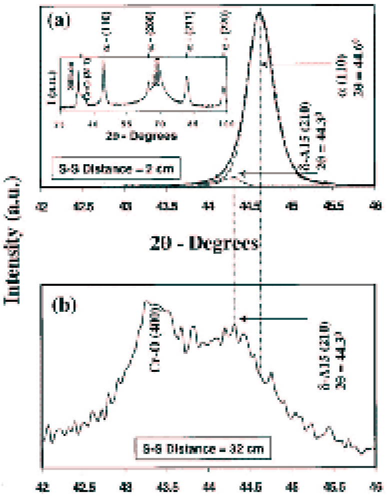

Figure 2. Strongest hkl region XRD spectra of chromium films deposited at SS distances of (a) 2 cm (inset: complete scan) and (b) 32 cm.

In conclusion, a sharp phase separation between δ-A15 and α-bcc chromium has been obtained using a close-distance, rapid evaporation where the temperature gradient as well as interfacial stress combined to achieve separation between nanophase chromium and bulk columnar grains. The observed suppression of the antiferromagnetic order and the rise in surface magnetization in nanophase chromium can be used to create layered, phase-separated structures with varying magnetic properties, where a single element system with changed properties can be used to replace multicomponent systems.

Reference

Saraf L, CM Wang, MH Engelhard, and DR Baer. 2003. "Temperature-Induced Phase Separation in Chromium Films." *Applied Physics Letters* 82**:**2230-2232.

Measurement of the Band Offsets between Amorphous $LaAlO_3$ and Silicon

L Edge,[(a)] D Schlom,[(a)] S Chambers,[(b)] E Cicerrella,[(c)] J Freeouf,[(c)] B Holländer,[(d)] and J Schubert[(d)]

(a) Pennsylvania State University, University Park, Pennsylvania
(b) Pacific Northwest National Laboratory, Richland, Washington
(c) Oregon Health and Sciences University, Portland, Oregon
(d) Institut für Schichten und Grenzflächen, Jülich, Germany

Currently, as SiO_2 approaches its fundamental limits, extensive research is being conducted to find alternative gate dielectrics to replace SiO_2 in metal oxide semiconductor field-effect transistors (MOSFETs). $LaAlO_3$ is a promising alternative gate dielectric. Single-crystalline $LaAlO_3$ has a dielectric constant of 24.1 ± 0.2 measured at 145 GHz and an optical bandgap of 5.6 eV. Amorphous $LaAlO_3$ thin films on silicon have an estimated dielectric constant of 20 to 25. It has also been shown that single-crystalline $LaAlO_3$ is stable in contact with silicon under standard MOSFET processing conditions of 1026°C for 20 seconds. The band offsets between $LaAlO_3$ and silicon have been predicted to be in the range 1.0 to 2.1 eV for electrons and 1.9 to 3.5 eV for holes. All of these properties meet the requirements for an alternative gate dielectric as suggested by the 2001 edition of the *International Technology Roadmap for Semiconductors* (Semiconductor Industry Association 2001).

Although $LaAlO_3$/silicon shows many promising properties, there are no published papers that have experimentally determined band offsets. It is critical that the high-K gate dielectric has conduction and valence band offsets ≥ 1 eV for both electrons and holes from the silicon. To this end, the band offsets between amorphous $LaAlO_3$ and silicon have been determined from x-ray photoelectron spectroscopy. These films, which are free of interfacial SiO_2, were made using molecular beam deposition at Pennsylvania State University. The band offsets were measured at W.R. Wiley Environmental Molecular Sciences Laboratory by researchers from Pennsylvania State University and Pacific Northwest National Laboratory (Edge et al. 2004). The band lineup is type I with measured band offsets of 1.86 ±0.2 eV for electrons and 3.23 ±0.1 eV for holes. Type I means that the band gap of silicon is entirely encased within the band gap of $LaAlO_3$, as shown in Figure 1. The band offsets are independent of the doping concentration in the silicon substrate as well as the $LaAlO_3$ film thickness, as seen in Table 1. These amorphous $LaAlO_3$ films have a band gap of 6.2 ± 0.1 eV, as measured by researchers from Oregon Health and Sciences University. The fact that the offsets at both band edges exceed 1 eV means that $LaAlO_3$ is a very attractive candidate for a next-generation gate oxide in silicon MOSFETs with low leakage current.

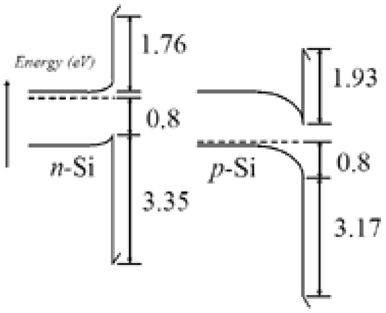

Figure 1. Type I means that the band gap of silicon is entirely encased within the band gap of $LaAlO_3$.

Table 1. Band offsets in silicon substrate and $LaAlO_3$ film.

Film	ΔE_c (eV)	ΔE_v (eV)
10 Å $LaAlO_3$/n-Si	1.75 ± 0.2	3.35 ± 0.1
10 Å $LaAlO_3$/p-Si	1.93 ± 0.2	3.17 ± 0.1
20 Å $LaAlO_3$/p-Si	1.99 ± 0.2	3.11 ± 0.1
40 Å $LaAlO_3$/n-Si	1.76 ± 0.2	3.34 ± 0.1
40 Å $LaAlO_3$/p-Si	1.88 ± 0.2	3.22 ± 0.1

References

Semiconductor Industry Association. 2001. *International Technology Roadmaps for Semiconductors: 2001*. San Jose, California.

Edge LF, DA Schlom, SA Chambers, E Cicerrella, JL Freeouf, B Holländer, and J Schubert. 2004. "Measurement of the Bond Offsets between Amorphous $LaAlO_3$ and Silicon." *Applied Physics Letters* 84:726-728.

Quantification of Trace Metals in Solids with Inhomogeneous Internal Structure Using Proton-Induced, X-Ray Emission

N Yadav,(a) S Maheswaran,(a) V Shutthanandan,(b) S Thevuthasan,(b) H Ngo,(c) and S Vigneswaran(c)

(a) University of Western Sydney, Sydney, Australia
(b) W.R. Wiley Environmental Molecular Sciences Laboratory, Richland, Washington
(c) University of Technology, Sydney, Australia

Granular activated carbon (GAC) is a highly porous material used to remove contaminants from drinking water via the process of adsorption. These contaminants, such as trace metals, adsorb to the surface of pores, which are randomly distributed within each GAC particle. To date, bulk analysis techniques used to directly quantify the adsorbed trace metals in GAC have been restricted to wet chemical techniques and neutron activation analysis (NAA). When wet chemical techniques such as atomic absorption spectrophotometry (AAS) and/or inductively coupled plasma mass spectrometry (ICP-MS) are used for the analysis of solid samples, samples require dissolution, decomposition, or extraction, steps that are laborious and introduce the risk of sample contamination. NAA avoids virtually all this sample preparation but only offers the highest sensitivities with a large amount of sample (5 to 10 g) that may not be available and a very high neutron flux (achievable only in a nuclear reactor). These two factors limit the use of NAA. A rapid, highly sensitive, non-destructive, multi-elemental analytical method is best suited for investigating the issues associated with trace elements. Proton-induced, x-ray emission (PIXE) is such a tool that can simultaneously quantify trace elements with sensitivities of at least parts per million.

In this project, we used GAC as an adsorbent to remove arsenic from water, and then used PIXE to measure the amount of adsorbed arsenic. The results were compared with the adsorbed amounts determined from atomic AAS measurements. Furthermore, the arsenic concentration measured by these techniques was used to construct various isotherms to study the total adsorption capacity of GAC. To simulate contaminated waters, we created a number of solutions using deionized and laboratory tap water supplemented with an arsenic stock solution. Equilibrium experiments were carried out with these solutions, and different adsorption mechanisms of arsenic in GAC were evaluated. These experiments were conducted in batches to allow easy manipulation and measurement of process variables. The samples in the equilibrium experiments consisted of between 0.1 g/L to 10.0 g/L of GAC added to a solution with an initial arsenic concentration of 4.9 mg/L. The GAC/arsenic mixture was then mixed for a period of 72 hours. After the mixing process, the GAC was isolated from the arsenic solution and analyzed using PIXE while arsenic remaining in the solution was measured using AAS. AAS measurements assumed that the amount of arsenic in the GAC was the initial amount of arsenic in the solution minus the arsenic left in the solution after treatment.

Arsenic concentration in GAC after equilibrium experiments using PIXE and AAS are shown in Figure 1. The differences between PIXE and AAS measurements are noticeable, and the PIXE results are higher than the AAS results. The area of the sample analyzed by PIXE may be the source of the differences in the result. Only two to three particles are being used as samples in the PIXE measurements. Microbeam PIXE measurements carried out on two arbitrarily chosen GAC particles clearly showed that different regions within each GAC particle adsorb different amounts of arsenic, and arsenic adsorption between the two particles is also different (the results for this part of the research are not provided). The sample examined by the PIXE beam might not have been representative for the whole sample.

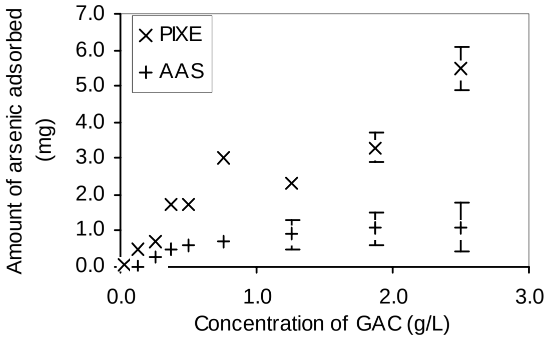

Figure 1. PIXE and AAS measurements of arsenic concentration in GAC after the equilibrium experiments.

Figure 2 shows the data from the equilibrium experiments fitted to a number of different isotherms. The results indicate that the AAS experimental data were reasonably consistent with the predictions of various isotherm models compared to the PIXE measurements. The inconsistency of PIXE data made the fitting of various isotherm models very difficult. The percentage error between experimental data and various isotherm models are quite high in the case of the PIXE data (20 to 80%) compared to AAS data (8 to 12%).

We have demonstrated that the PIXE technique can be effectively used to determine trace arsenic concentration in GAC. However, inhomogeneous structures of GAC make it difficult to obtain consistent AAS values.

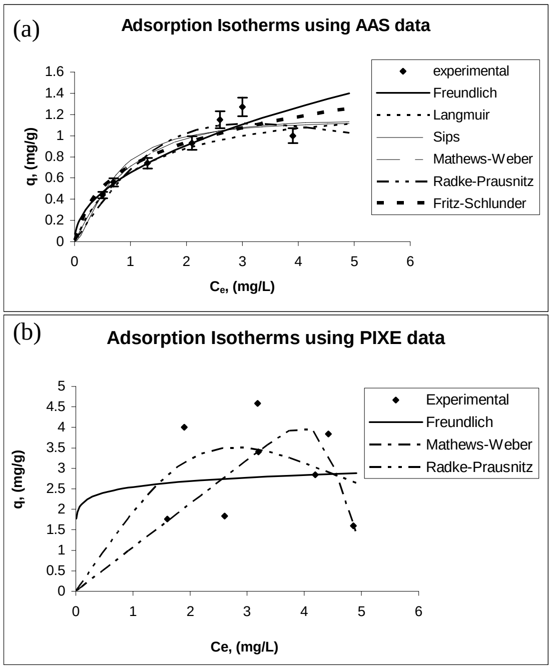

Figure 2. Various adsorption isotherm models fitted to (a) AAS and (b) PIXE data. The term q is the adsorption density at the equilibrium solute concentration C_e [mg of adsorbate per g of adsorbent, and C_e is the concentration of adsorbate in solution (mg/L)].

Reactions at Interfaces as a Source of Sulfate Formation in Sea-Salt Particles

A Laskin,[a] D Gaspar,[a] W Wang,[b] S Hunt,[b] J Cowin,[c] S Colson,[c]
and B Finlayson-Pitts[b]
(a) W.R. Wiley Environmental Molecular Sciences Laboratory, Richland, Washington
(b) University of California, Irvine, California
(c) Pacific Northwest National Laboratory, Richland, Washington

Understanding the formation of sulfate particles in the troposphere is critical because of their health effects and direct and indirect effects on radiative forcing, hence on climate. Laboratory studies of the chemical and physical changes in NaCl, the major component of sea-salt particles, show that NaOH is generated upon reaction of deliquesced NaCl particles with gas phase OH. The increase in alkalinity will lead to an increase in the uptake and oxidation of SO_2 to sulfate in sea salt particles. Atmospheric models typically overestimate the amount of SO_2 and underestimate the amount of sulfate near the earth's surface. The explanation for this discrepancy may lie in the chemistry of sea-salt particles thrown into the atmosphere by wind and waves. Using particles of NaCl, researchers at Pacific Northwest National Laboratory have demonstrated that salt can react with atmospheric hydroxyl radicals (formed from the reaction of ozone, light, and water vapor) to produce NaOH, which is shown coating a salt particle in Figure 1. The NaOH increases the pH of the salt particles, and the alkalinity in turn promotes the oxidation of SO_2 by ozone to yield sulfate. In a publication of this work (Laskin et al. 2003), the researchers noted, "This chemistry is missing from current models, but is consistent with a number of previously unexplained field observations."

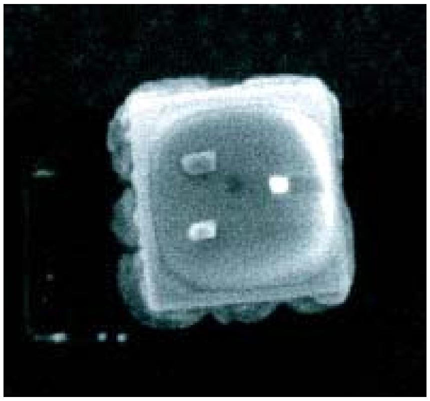

Figure 1. An image of NaOH coating an NaCl particle obtained using the environmental scanning electron microscope in the W. R. Wiley Environmental Molecular Sciences Laboratory's Chemistry & Physics of Complex Systems Facility. This image was recently published in Science (Laskin et al. 2003).

Reference

Laskin A, DJ Gaspar, W Wang, SW Hunt, JP Cowin, SD Colson, and BJ Finlayson-Pitts. 2003. "Reactions at Interfaces as a Source of Sulfate Formation in Sea-Salt Particles." *Science* 301:340-344.

Surface Decontamination of Simulated Chemical Warfare Agents Using a Nonequilibrium Plasma with Off-Gas Monitoring

T Moeller,(a) M Alexander,(b) M Engelhard,(c) D Gaspar,(c) M Luna,(a) and P Irving(a)
(a) InnovaTek, Inc., Richland, Washington
(b) Pacific Northwest National Laboratory, Richland, Washington
(c) W.R. Wiley Environmental Molecular Sciences Laboratory, Richland, Washington

An effective, near-real-time decontamination system for toxic chemical and biological materials on surfaces will address a range of concerns in the military and industrial sectors. These concerns include protecting troops and civilians against chemical and biological agents on the battlefield or in terrorist situations, or ensuring sanitation in the food-processing industry. InnovaTek, Inc., is developing a surface decontamination technology that uses active species generated in a nonequilibrium corona plasma. In this project, InnovaTek staff members used a variety of instrumental methods available in the W.R. Wiley Environmental Molecular Sciences Laboratory to verify the efficacy of the plasma technology. These methods included gas chromatography-mass spectrometry (GC MS), x-ray photoelectron spectroscopy (XPS), and secondary ionization mass spectrometry (SIMS). Ion trap mass spectrometry (ITMS) with direct atmospheric sampling was used as a real-time monitor of the decontamination process.

The plasma technology was tested against DMMP, a simulant for the chemical agent Sarin. Test coupons made from flat pieces of aluminum with a surface area of approximately 4 cm^2 were thoroughly cleaned and then inoculated with 5 μL droplets of DMMP at a minimum concentration of 0.5 g/m^2. Immediately after inoculation, the test coupons were exposed to the plasma for periods ranging from 1 to 20 minutes. To determine the quantity of DMMP remaining on the surface of the coupon vs. plasma treatment time, the coupons were rinsed with acetone at varying time intervals, and the solution was analyzed with GC MS. The data shown in Figure 1 indicate that greater than a 4-log$_{10}$ destruction of the DMMP on the aluminum surface was achieved after a 10-min plasma treatment.

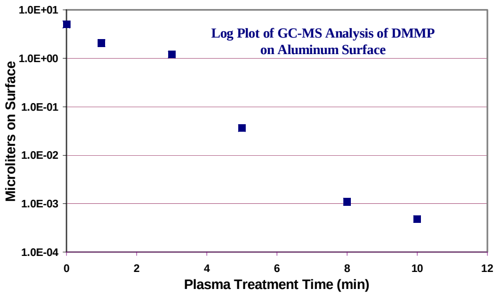

Figure 1. Chemical agent decontamination efficiency for DMMP, a Sarin simulant, on an aluminum surface treated with a 20-Watt plasma flare prototype.

Additional information about the plasma decontamination process was obtained by real-time monitoring of the gas-phase products using an ITMS with a direct air-sampling interface. Figure 2 shows the relative concentration vs. exposure time for the primary peaks observed in the mass spectrum, PO_3 and PO. The relative concentration of the DMMP breakdown products from plasma exposure shows a range of approximately two orders of magnitude. These data are consistent with the GC MS results, although the dynamic range is reduced on the low end by signal-to-noise limitations and on the high end by the time response of the system. The apparent induction time of two minutes is a convolution of the actual induction time for the DMMP on the surface to react with the plasma and the delay and broadening caused by the capillary interface. These factors have the effect of spreading the intensity in time and reducing the maximum observed signal. The difference between the off-gas mass spectrum and the pure DMMP mass spectrum is significant because it demonstrates unequivocally that the cold plasma decontamination process is reducing the DMMP to harmless components, not simply volatilizing it.

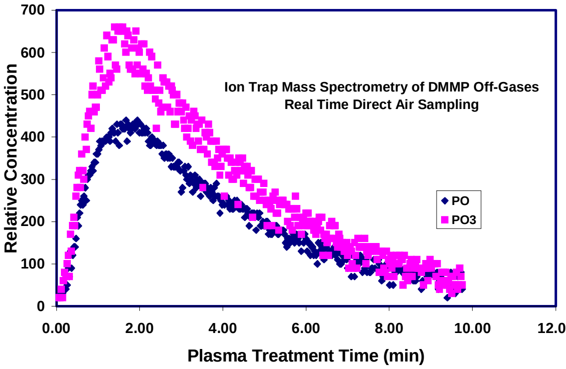

Figure 2. Analysis of off-gases during the decontamination of DMMP on an aluminum surface treated with a 20-Watt plasma.

GC MS analysis showed that a greater than 4-log_{10} destruction of the DMMP on an aluminum surface was achieved in a 10-min treatment. XPS and SIMS were used to detect any trace levels of the simulated contaminant, and the XPS and SIMS data were consistent with the GC MS data, indicating that less than a monolayer of DMMP remained after plasma treatment. Figure 3 shows SIMS data that demonstrate the changes in surface chemistry produced by exposure to the plasma. The technology is being further refined to develop a product that will not only decontaminate surfaces but will also sense when decontamination is complete.

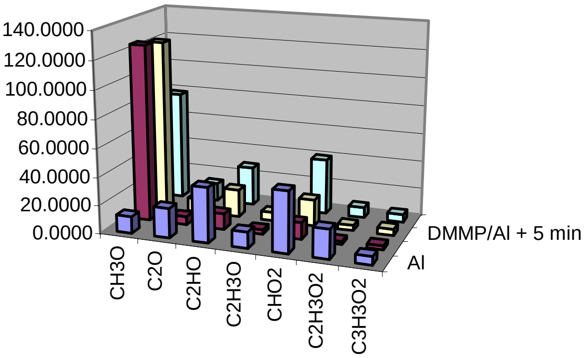

Figure 3. SIMS results for selected chemical fragments resulting from plasma treatment of a test coupon and an aluminum control coupon.

Improved Catalysts for the Non-Thermal Plasma-Assisted Catalytic NO_x Reduction

J Kwak,[(a)] *J Szanyi,* [(a)] *and C Peden*[(a)]
(a) Pacific Northwest National Laboratory, Richland, Washington

Improving the fuel economy of internal combustion engines is the driving force behind changes in engine operating conditions. One way to improve engine performance is to provide excess oxygen for combustion (i.e., operate the engine under "lean" conditions). Currently, only diesel engines operate under true lean conditions all the time. Lean engine operation, however, makes NO_x removal from an oxygen-containing, exhaust-gas mixture a very challenging task. Traditional three-way catalysts containing precious metals are unable to remove NO_x under lean conditions. Zeolite-based, primarily transition-metal ion exchanged catalysts have been extensively studied in the last two decades for the selective catalytic reduction of NO_x. Insufficient activities, narrow operating windows, and the sensitivity of these materials to water and sulfur poisoning have hindered their practical application.

When a non-thermal plasma was applied in front of the catalyst bed, alkali and alkaline earth ion exchanged Y,FAU (Y) zeolites have shown promising catalytic activities for the removal of NO_x. In the absence of the non-thermal plasma, these materials show no catalytic activity toward the decomposition of NO_x. Over the catalyst bed, the NO_2 formed in the plasma undergoes selective catalytic reduction by the partially oxidized hydrocarbons, which also are formed in the plasma reactor.

The effect of the ion-exchange method on the NO_x reduction activity of a Ba-Y catalyst has been reported previously (Eberling et al. 2001). The activity of a Ba-Y catalyst prepared by aqueous solution ion exchange was higher than the one that was solid-state ion exchanged with a chloride salt. The different activities of these two catalysts were explained by the differences in their acidities. The solution ion exchanged Ba-Y was shown to have higher acidity, making it a better catalyst for hydrocarbon activation. However, this catalyst was prone to deactivation as a result of coke formation on the acidic sites, while no deactivation was observed on the solid-state ion exchanged Ba-Y.

The effects of catalyst preparation on the NO_x reduction activity of a series of Ba-Y,FAU zeolites were investigated using a simulated exhaust gas mixture (Kwak et al. 2003). We have previously shown that the introduction of Ba^{2+} ions into Na-Y,FAU results in a large increase in their non-thermal, plasma-assisted NO_x reduction activity. The NO_x reduction activities of Ba-Y,FAU catalysts were found to increase with increasing Ba^{2+} concentration in the aqueous ion exchange solutions, which translated into increased Ba^{2+}/Na^+ ratios in the resulting materials. Consecutive ion exchange procedures using an excess of Ba^{2+} in aqueous solution, however, did not improve the NO_x reduction activities of Ba-Y, FAU catalysts (i.e., the activity of a material that was ion exchanged four times was the same as that of the material that was exchanged only once). In contrast, a significant increase in NO_x reduction activity was observed when a 773 K calcination step was implemented after each solution ion exchange as shown in Figure 1. Calcination that followed each ion exchange step seems to further increase the Ba^{2+}/Na^+ ratio in the zeolite and, in turn, to increase the NO_x

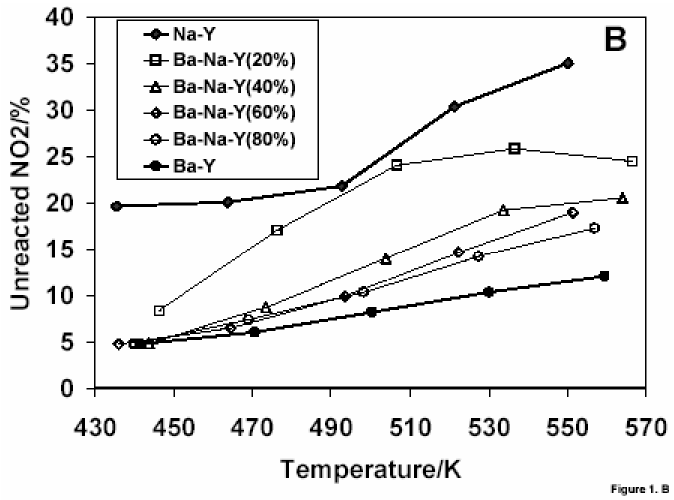

Figure 1. The effect of multiple ion exchange/calcination on the NO_x conversion (A) and unreacted NO_2 levels at the exit end of the reactor (B) over Ba(Na)-Y,FAU catalysts. [filled diamonds: Na-Y; open squares: Ba-Y(1-1); open triangles: Ba-Y(2-2); open circles: Ba-Y(3-3); filled circles: Ba-Y(4-4)].

reduction activities of the catalysts prepared this way. Key differences in Na-, and Ba-Y catalysts were found in NO_2 adsorption and temperature-programmed desorption experiments; notably, Ba-Y chemisorbs NO_x much stronger than Na-Y.

References

Eberling AC, AA Panov, DE McCready, and ML Balmer. 2001. "Characterization of Acid Sites in Ion-Exchanged and Solid State-Exchanged Zolites." Reprinted from *Non-Thermal Plasma Emission Control Systems* (SP-1639), Society of Automotive Engineers, Warrendale, Pennsylvania.

Kwak J, J Szonyi, and CHF Peden. 2003. "Nonthermal Plasma-Assisted Catalytic No_x Reduction Over Ba-Y, FAU: The Effect of Catalyst Preporation." *Journal of Catalysis* 220:291-298.

Proton Transfer Reaction Ion Trap Mass Spectrometry

M Alexander,[(a)] *P Prazeller,*[(b)] *T Jobson,*[(a)] *and P Palmer*[(b)]
(a) Pacific Northwest National Laboratory, Richland, Washington
(b) San Francisco State University, San Francisco, California

Proton transfer reaction mass spectrometry (PTR-MS) is a relatively new field that has attracted a great deal of interest in the last several years. This technique uses H_3O^+ as a chemical ionization agent. The advantages of PTR-MS include high sensitivity, selectivity, and accuracy. A commercial PTR-MS was purchased in fiscal year 2001 for the W.R. Wiley Environmental Molecular Sciences Laboratory (EMSL). The PTR-MS mass spectra are simpler than those obtained by conventional electron-impact spectra because the ionization method, transfer of a proton, is "soft," thus little fragmentation occurs. This feature, however, can cause problems in peak identification because of isobaric interferences. A possible solution to this problem is to couple the PTR drift tube to an ion trap mass spectrometer (ITMS). This possible solution has been the subject of much speculation and discussion in the PTR-MS community. ITMS is appealing because of its ability to perform tandem mass spectroscopy (MS-MS) analysis and possibly to distinguish between isomers and other isobars. It is also appealing because the duty cycle is much higher than a linear quadrupole so faster time response can be obtained for the detection of multiple compounds. This project represents the first successful effort in creating a PTR-ITMS.

We have constructed a prototype instrument using a drift tube from the EMSL commercial PTR-MS (Ionicon) and a Finnegan Saturn ITMS. A schematic is shown in Figure 1. The interface is designed to replace the standard electron gun and uses a simple Einzel lens to focus the ions from the drift tube exit into the ITMS. The goal here was not to achieve the ultimate sensitivity, but to determine the efficiency of ion injection and to understand how to improve sensitivity in a second-generation instrument. The operating pressures are 1 to 2 Torr in the drift tube, 0.1 Torr in the interface, and 5×10^{-4} Torr in the ion trap. We determined that an ion current of 200pA makes it through the interface to the entrance aperture for the ion trap and about 1% of those ions are stored and detected in the ITMS. Under these conditions the detection limit was found to be 10 ppm. Although this is hardly an impressive number, there are several issues that can be addressed to dramatically improve the sensitivity.

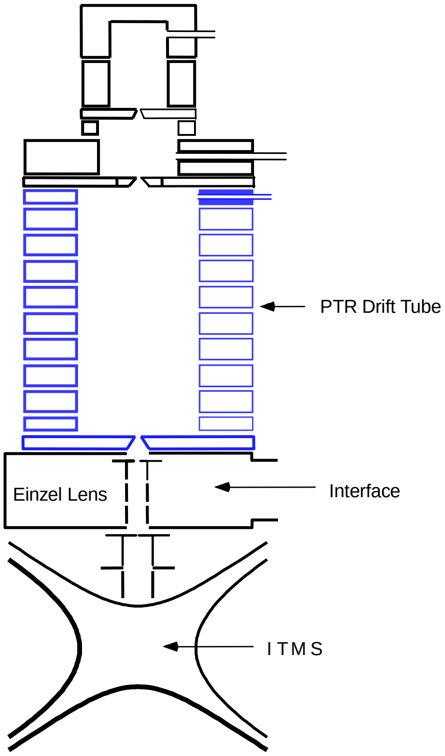

Figure 1. Schematic of PTR-ITMS showing the drift tube, interface, and ITMS.

The first issue is that the trap had to be run at high pressure to compensate for the high ion energies required to make the ion pass through the interface. This operating requirement resulted in a background level at least a factor of 100 higher than is normal for this detector. Simply implementing differential pumping can improve the sensitivity by a factor of 100, and better pumping in the interface can improve the signal by a factor of 10 to 100. Implementing these features should result in sensitivities of 1 ppb or better. The other issue is how effective MS-MS in an ion trap will be in distinguishing isobars—for example, acetone and propanal, both of which have a protonated mass of 59. Figure 2 shows that both compounds fragment into mass 41 and mass 31, but with different fragmentation ratios. These data indicate that MS-MS in the ITMS could distinguish between pure compounds, but mixtures would be hard to resolve.

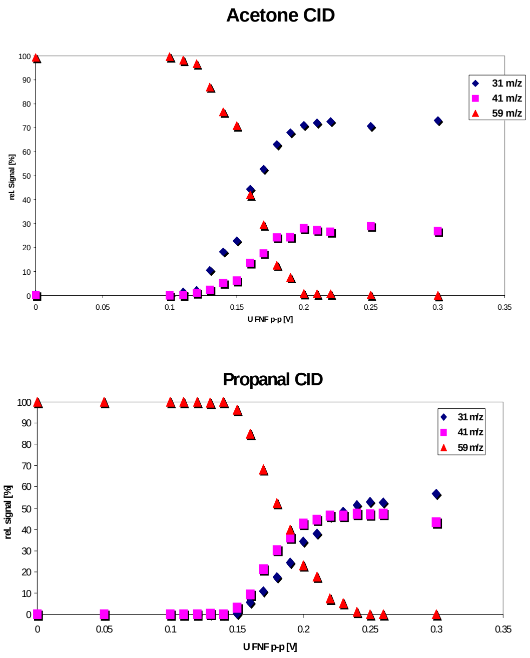

Figures 2. MS-MS spectra of protonated acetone (top) and propanal (bottom) as a function of excitation voltage.

The data to date show a great deal of promise for PTR-ITMS. The sensitivity should ultimately be 1 ppb or better which, combined with the higher duty cycle inherent in ITMS, will make the PTR-ITMS a valuable tool for time-dependent studies. MS-MS can be a valuable tool for distinguishing between some isobars of protonated species.

Heteroepitaxial Growth of a Manganese Carbonate Secondary Nano-Phase on the $(10\bar{1}4)$ Surface of Calcite In Solution

A Lea,[a] *T Hurt,*[b] *A El-Azab,*[c] *J Amonette,*[c] *and D Baer*[c]

(a) W.R. Wiley Environmental Molecular Sciences Laboratory, Richland, Washington
(b) Cornell University, Ithaca, New York
(c) Pacific Northwest National Laboratory, Richland, Washington

The prominence of carbonates in mineral-interface studies arises from their simple structures, highly dynamic surface chemistry, and abundance in natural systems ranging from terrestrial soils and sediments to aquifers and marine deposits. Carbonates are able to adsorb and co-precipitate with metallic cations and oxyanions of environmental importance and geological interest. The rates at which they nucleate, precipitate, dissolve, and act to adsorb and incorporate ionic species have a strong effect on the transport of contaminants in groundwater systems. Such processes involve transfer of mass and energy across the aqueous-mineral interface and depend strongly on the molecular-scale details of the carbonate surface.

A vast amount of literature treats the interaction of metallic cations or oxyanions with calcite, the most prevalent carbonate mineral. These impurity studies have shown that calcite is a highly reactive mineral that undergoes a variety of surface reactions in solution. These reactions significantly affect the concentration of metallic cations and oxyanions in calcareous systems. Yet despite the preponderance of impurity investigations on this mineral, only recently has evidence of heteroepitaxial growth on calcite been reported. Here, we examine the formation of a Mn-rich carbonate phase that has been observed to grow epitaxially on an otherwise dissolving calcite surface.

Specifically, we consider the conditions under which these precipitates form, as well as their growth behavior and structural characteristics. The composition of these precipitates has been deduced from bulk solution species measurements in conjunction with spectroscopic data and thermodynamic calculations. The growth characteristics have been explained in terms of the fine structure of surface steps, the mechanism of step motion on the surface, and the theoretical framework for epitaxial growth governed by surface energy and relative elasticities of the growing phase and substrate. Lattice mismatch, along with elasticity parameters for the substrate and film, are used to derive the cross-sectional profile of these epitaxially strained precipitates using a glued-wetting-layer model that gives the equilibrium island profile in terms of the elastic and surface energy of the growing phase.

Heteroepitaxy of a manganese carbonate phase with nanometer dimensions on the $(10\bar{1}4)$ surface of calcite ($CaCO_3$) using atomic force microscopy (AFM) has been observed in solution during dissolution of calcite when the ion activity product of Mn^{2+} and CO_{2-3} nears the solubility limit of $MnCO_3$. Growth rate observations at different Mn concentrations, coupled with x-ray photoelectron spectroscopy and electron paramagnetic resonance measurements, suggest that the resulting phase is $Mn_{0.5}Ca_{0.5}CO_3$. These islands, while growing many microns in length along the $[2\bar{2}1]$ direction, have a uniform width in the range of 120 to 240 nm and a uniform height of approximately 2.7 nm, which corresponds to nine atomic layers. The islands stop growing when they encounter step edges and have been observed to dissolve when undercut by a growing etch pit (Figure 1).

Comparison of the crystal lattices of calcite and $Mn_{0.5}Ca_{0.5}CO_3$ indicates that $[2\bar{2}1]$ is the direction of preferred growth. A glued-wetting-layer model with a condition of constant surface chemical potential has been used to model the observed cross section of the heteroepitaxial layer. Although not all the required parameters are accurately known, the model accurately depicts the measured profiles of the islands (Lea et al. 2003).

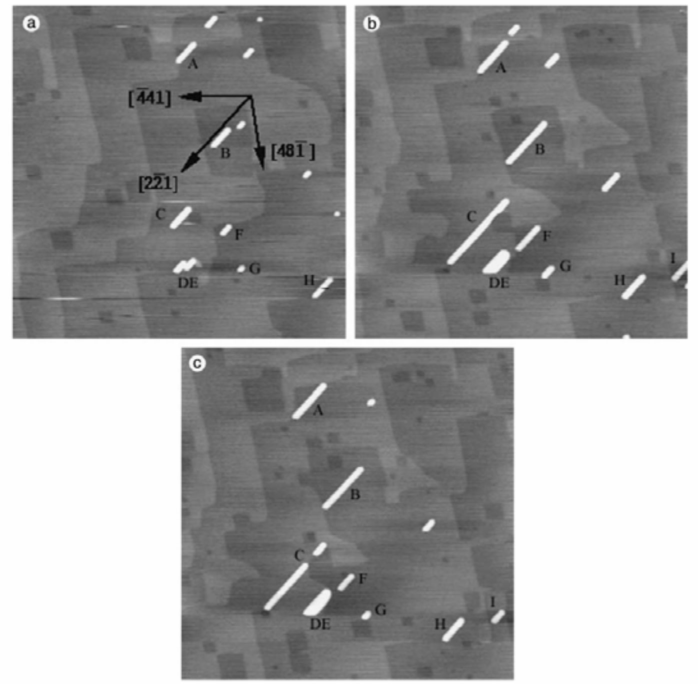

Figure 1. AFM topographic images of the $(10\bar{1}4)$ surface of calcite in a pH-8.9, 150-μM carbonate solution containing 2 μM Mn^{2+}. Visible in the images are 3.14 Å single steps, single- and multilayer deep etch pits, and highly oriented precipitates on the surface of calcite. Images (b) and (c) were 11 and 26 minutes after the first image (a). Superimposed on image (a) are the principal crystallographic axes on the calcite surface.

Reference

Lea AS, TT Hurt, A El-Azab, JE Amonette, and DR Baer. 2003. "Heteroepitaxial Growth of a Manganese Carbonate Secondary Nano-Phase on the $(1\bar{1}04)$ Surface of Calcite in Solution." *Surface Science* 524:63-77.

Selective Formation of Single-Phase Oxide Nanoclusters: Cu_2O on $SrTiO_3(100)$

I Lyubinetsky,[a] S Thevuthasan,[a] and D Baer[b]
(a) W.R. Wiley Environmental Molecular Sciences Laboratory, Richland, Washington
(b) Pacific Northwest National Laboratory, Richland, Washington

Synthesis of three-dimensional nanostructures such as nanoclusters of metals and semiconductors results in formation of quantum dots possessing novel electronic and optical properties derived from the quantum confinement of charge carriers. Nanoscaled clusters also attract interest with respect to phase transitions, which may be different from that observed in bulk due to the increase of the surface-to-bulk ratio. Oxides constitute a highly diverse class of materials with rich optical, electronic, magnetic, and dielectric properties, and as such, have significant technological potential. Cuprous oxide (Cu_2O) is of considerable interest because of its unique electronic structure, and also its evolving potential in chemical and photochemical applications, in particular, water splitting. We have evaluated experimental parameters for the formation of single-phase Cu_2O nanoclusters on the $SrTiO_3(001)$ surface in terms of the pressure-temperature phase diagram. The Cu_2O nanoclusters were synthesized using oxygen plasma-assisted molecular beam epitaxy. The chemical state information from the surface region of the nanoclusters was acquired using *in situ* x-ray photoelectron spectroscopy (XPS) and x-ray induced Auger electron spectroscopy (AES). *Ex situ* analysis was performed using an atomic force microscope (AFM) to map the morphology of the clusters.

Since copper has multiple oxidation states, the chemical state of the synthesized nanoclusters should be verified. Figure 1 presents the Cu $2p_{3/2}$ core level x-ray photoelectron [Figure 1(a)] and Auger Cu L_3VV spectra [Figure 1(b)] from samples containing copper in all three different charge states. The 2p peak binding energy difference between Cu^{2+} and Cu^{1+} (in Cu_2O) is quite large ($\Delta E \sim 1.6$ eV) and can be clearly resolved in an XPS spectrum containing a mixture of Cu^{1+} and Cu^{2+} [Figure 1(a)]. Meanwhile, it is difficult to resolve the peaks due to Cu^0 and Cu^{1+} in XPS spectra. Cu and Cu_2O Auger peaks are well separated in AES, as shown in Figure 1(b). The major Cu L_3VV Auger peaks, associated with Cu^0 and Cu^{1+}, have kinetic energies of 918.8 and 916.4 eV, respectively. Analyzing the experimental parameters for the Cu_2O nanocluster formation, a phase diagram as a function of growth temperature and oxygen pressure under constant Cu flux has been determined and is shown in Figure 2. For comparison purposes, Figure 2 also displays the bulk Cu-O phase diagram.

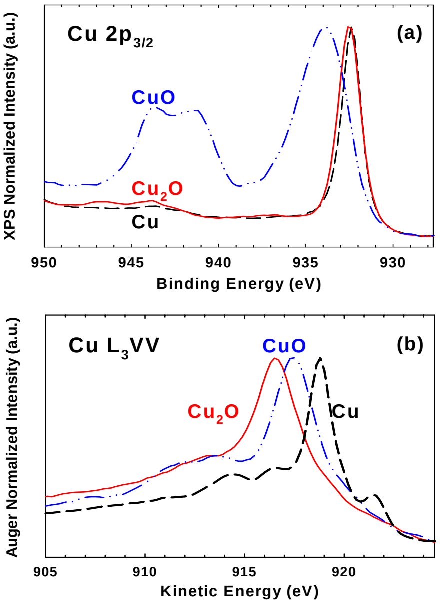

Figure 1. XPS Cu $2p_{3/2}$ (a) and AES Cu L_3VV (b) spectra of CuO, Cu_2O, and Cu.

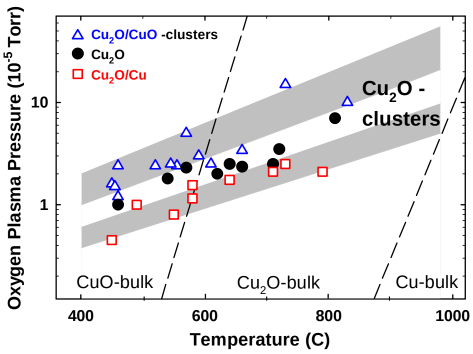

Figure 2. Phase diagram for the formation of the copper oxide nanoclusters on $SrTiO_3$.

It is remarkable that a region associated with the growth of pure Cu_2O nanoclusters is observed to be very narrow, especially when compared to the bulk Cu-O phase diagram, making it quite a challenge to achieve the formation of the nanodots containing a single phase of cuprous oxide. In the temperature range studied (450 to 850°C), the corresponding oxygen pressure region covers just less than the order of magnitude for nanoclusters vs. more than six orders for bulk Cu_2O. Another notable observation is the two distinctive mixed phase bands in phase space for the nanoclusters. The band observed at higher oxygen pressure than is required for pure Cu_2O growth (Figure 2) contains Cu in two different charge states of Cu^{1+} and Cu^2, while Cu^{1+} and Cu^0 are observed in the second band at lower pressures. It is considerably different from the bulk, that outside the fine Cu_2O region in the phase diagram for the nanoclusters, there are bands of temperature and pressure within which two phase-like forms coexist, not as the rather sharp phase boundaries observed for the bulk. This finding may be considered to be experimental confirmation of the theoretical prediction of multiphase coexistence bands for the small systems, which is the consequence of the small differences between the free energies of clusters in different phase-like forms.

Formation of nanoclusters on $SrTiO_3$(100) has been observed at all growth parameters studied, but structural details have been found to depend on the island composition. For the same amount of deposited Cu, Figure 3 illustrates the typical morphologies observed for different regions of the phase diagram. For pure Cu_2O [Figure 3(a)], the morphology consists of isolated small (20 to 50 nm lateral dimensions) square/rectangular clusters with flat tops, oriented mostly along the same <100> direction, which indicates a crystalline ordering and epitaxy. For the Cu_2O/CuO region [Figure 3(b)], there is a coexistence of the similar small, and the large (100 to 150 nm) more round clusters, which indicate possible phase-like separation for the cuprous and cupric oxides. In contrast, there are only minor changes in the morphology for the Cu_2O/Cu region; in particular, in Figure 3(c), a slight reduction of the square cluster size (10 to 40 nm) with simultaneous increase of quantum dot density was observed.

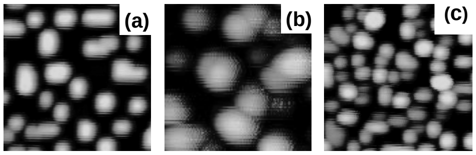

Figure 3. AFM 300 nm × 300 nm × 20 nm images for nanoclusters grown at 600°C at oxygen pressure of (a) 1.5×10^{-5} Torr, (b) 3.5×10^{-5} Torr, and (c) 9.0×10^{-6} Torr.

Oxygen Analysis Using Ion Beam Methods

W Jiang,(a) V Shutthanandan,(b) S Thevuthasan,(b) D McCready,(b) and W Weber(a)
(a) Pacific Northwest National Laboratory, Richland, Washington
(b) W.R. Wiley Environmental Molecular Sciences Laboratory, Richland, Washington

Nuclear reaction analysis (NRA) complements the widely used Rutherford backscattering spectrometry (RBS) and is the preferred method used to analyze light elements on or near the surface of a compound containing heavy elements. There are many prominent features of NRA, including high selectivity of isotopes, good sensitivity for many nuclides, non-destructive depth profiling, and quantitative analysis of elemental concentrations. Using a thin amorphous layer of SiO_2 (5.2 μg/cm^2) on Si, cross sections for the nuclear reactions $^{16}O(d,p_1)^{17}O$, $^{16}O(d,\alpha)^{14}N$ and $^{16}O(\alpha,\alpha)^{16}O$ at a laboratory angle of 150° were determined over energies ranging from 0.701 to 1.057 MeV for D^+ ions and from 2.949 to 3.049 MeV for He^+ ions.

Based on a calibration of the thickness-corrected data using a reference point of 4.42 mb/sr at E_d = 0.886 MeV and θ_{Lab} = 150°, the absolute values of the cross section for the $^{16}O(d,p_1)$ reaction were obtained. These values are shown in Figure 1 as a function of the primary D^+ energy E_d. Also included in the figure are the results reported by Amsel and Samuel (1967) for the excitation curve at θ_{Lab} = 150°. In general, there is an excellent agreement between the two data sets. From Figure 1, there is a monotonic increase of the cross section with increasing D^+ energy from 0.701 to 0.774 MeV. A plateau-like structure appears between 0.774 and 0.926 MeV on the excitation curve. The average value of the cross section in this energy range corresponds to 4.56 mb/sr with a fluctuation of ~10%. From 0.926 MeV to 1.057 MeV, there is a broad resonant peak with the maximum intensity of ~12.1 mb/sr at 0.979 MeV and a full width at half maximum (FWHM) of 95 keV. The energy width (152 keV) of the plateau corresponds to a detectable depth of over 1 μm for most oxide materials, such as $SrTiO_3$, based on the SRIM2000 database. For conventional ion-beam analysis using a surface-barrier detector, this cross section plateau is not strongly recommended for profiling ^{16}O, as the depth resolution is poor (on the order of 100 nm).

Figure 2 shows the excitation curve from this study for the reaction $^{16}O(d,\alpha)^{14}N$ at θ_{Lab} = 150° over energies ranging from 0.701 to 1.057 MeV. The thickness-corrected relative cross sections were normalized for 5.07 mb/sr at E_d = 0.901 MeV. This calibration is based on the average value of the cross sections of 4.40 mb/sr at 135° and 5.75 mb/sr at θ_{Lab} = 165°, since there is no data available at θ_{Lab} = 150° for the reaction. Also included in Figure 2 is the reported data at θ_{Lab} = 145° from 0.750 to 0.950 MeV. In general, both curves show an increase in cross sections with increasing ion energy over the energy range, and the rates of increase are comparable. The result from this study also shows a broad resonance that appears between 0.96 and 1.06 MeV with the maximum cross section of 9.56 mb/sr at 1.004 MeV. Because the cross section of the $^{16}O(d,\alpha)$ reaction varies slowly with ion energy between 0.8 and 0.9 MeV, it has been used for depth profiling of oxygen in SiO_2 layers up to 600 nm in depth.

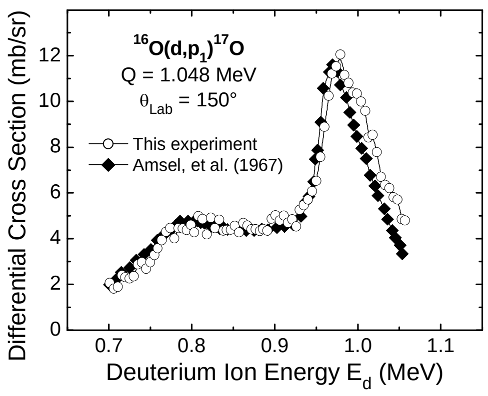

Figure 1. Cross sections for the reaction $^{16}O(d,p_1)^{17}O$ at θ_{Lab} = 150° as a function of ion energy. Also included are the data at the same reaction angle from Amsel and Samuel (1967).

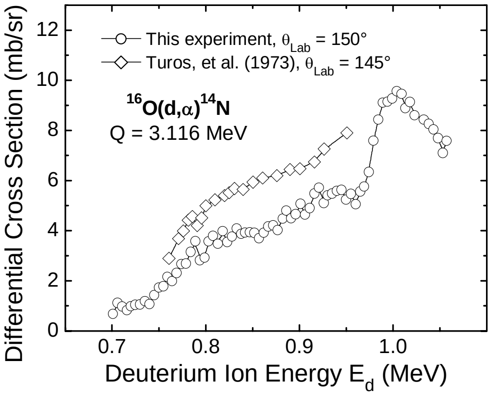

Figure 2. Cross sections for the reaction $^{16}O(d,\alpha)^{14}N$ at θ_{Lab} = 150° as a function of ion energy. Also included are the data at θ_{Lab} = 145° from Turos et al. (1973).

For He^+ elastic scattering from ^{16}O, the cross section data for θ_{Lab} = 150° are plotted in Figure 3. There is only a gradual increase over the energy range from 2.95 to 3.01 MeV, followed by a sharp nuclear resonant peak at 3.030 ±0.005 MeV (with a FWHM of ~12 keV) that is consistent with the report by Leavitt et al. (1990). The maximum cross section at the peak corresponds to $8.54\sigma_R$. This strong, narrow, and isolated nuclear resonance of $^{16}O(\alpha,\alpha)$ is recommended for depth profiling of ^{16}O. Based on the FWHM of the peak, the depth resolution corresponds to 34 and 48 nm for ^{16}O analysis in the near-surface region of $SrTiO_3$ and SiO_2, respectively.

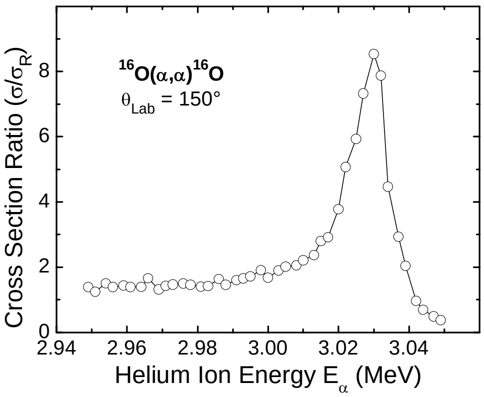

Figure 3. Cross sections for the scattering $^{16}O(\alpha,\alpha)^{16}O$ at θ_{Lab} = 150° as a function of ion energy.

References

Amsel G and D Samuel. 1967. “Microanalysis of the Stable Isotopes of Oxygen by Means of Nuclear Reactions.” *Analytical Chemistry* 39:1689-1698.

Leavitt JA, LC McIntyre Jr., MD Ashbaugh, JG Oder, Z Lin, and B Dezfouly-Arjomandy. 1990. “Cross Sections for 170.5° Backscattering of 4He from Oxygen for 4He Energies between 108 and 5.0 MeV.” *Nuclear Instruments and Methods in Physics B* 44:260-265.

Turos A, L Wielunski, and A Barcz. 1973. “Use of the Nuclear Reaction $^{16}O(d,\alpha)^{14}N$ in the Microanalysis of Oxide Surface Layers.” *Nuclear Instruments and Methods* 111:605-610.

User Projects

Investigation of Oxygen Diffusion in Single Crystal STO Films Grown on Si

ZJ Yu

Motorola, Inc., Tempe, Arizona

Fabrication of Microconduits

G Dunham

Pacific Northwest National Laboratory, Richland, Washington

Development of Advanced Durable Lean NOx Catalysts for Diesel Engine After Treatment

PW Park, K Koshkarian

Caterpillar, Inc., Peroria, Illinois

Analysis of Gases Produced During Plasma Treatment of Surfaces Contaminated with Chemical and Biological Agent Simulants

TM Moeller, M Fountain, L Allen

Innovatek, Inc., Richland, Washington

XRD Analysis of Inorganic Chemicals

LL Reed, AF Fuciarelli

Battelle Columbus, Richland, Washington

Deposition of High-K Dielectric Thin Films

AC Tuan

University of Washington, Seattle, Washington

Ceria-Zirconia, Thin-Film Crystals for Electron Microscopy Studies of Metal-Support Interactions in Model Automotive-Exhaust Catalysts

GW Graham

Ford Motor Company, Dearborn, Michigan

Biogenic Iron Materials

YA Gorby, AC Dohnalkova

Pacific Northwest National Laboratory, Richland, Washington

Interaction of Water and Formic Acid with Oxide Surfaces

LN Wang

Pacific Northwest National Laboratory, Richland, Washington

Post-Growth Analysis of GaN and InGaN Grown with MOCVD

K Poochinda, T Chen

University of Washington, Seattle, Washington

Crystal Perfection in Cadmium-Zinc-Telluride Radiation Detectors

M Bliss

Pacific Northwest National Laboratory, Richland, Washington

Examination of Failed Capscrew, Metallic Debris, Element Identification

JR LaSalle

Energy Northwest, Richland, Washington

Materials for Automotive Sensor Development

GW Coffey

Pacific Northwest National Laboratory, Richland, Washington

Denox Reactions on Ceria and Zirconia-Modified Ceria

JA Rodriguez, J Hrbek, G Liu

Brookhaven National Laboratory, Upton, New York

Chemistry of Cadmium-Zinc-Telluride Surfaces After Processing

AA Rouse

eV Products, Saxonburg, Pennsylvania

MeV He Ion Implantation in Si Wafers

FS Ohuchi

University of Washington, Seattle, Washington

Gold Implantation and Subsequent Formation of Gold Nano-Clusters on Glass Samples

SK Sundaram

Pacific Northwest National Laboratory, Richland, Washington

Field Emission Microscopy of Calcium Phosphate Films

BJ Tarasevich

Pacific Northwest National Laboratory, Richland, Washington

XRD Data Analysis and Consultation

ME Bussell

Western Washington University, Bellingham, Washington

Characterizations of Niau Bimetallic Butane Steam Reforming Catalyst

Y Chin

Pacific Northwest National Laboratory, Richland, Washington

Synthesis, Characterization, and Evaluation of Molybdenum Phosphide Hydrodesulfurization Catalysts

DC Phillips, DH Shorten, ME Bussell, SJ Sawhill, J King, AW Burns, M Pease, KA Layman, DR Van Wyk
Western Washington University, Bellingham, Washington
CH Peden
Pacific Northwest National Laboratory, Richland, Washington

XPS Studies of Nickel Cobalt Oxide Films

CF Windisch
Pacific Northwest National Laboratory, Richland, Washington

X-Ray Photoelectron Spectroscopic Study of Chemical Bonding and Electronic Structures of the Al_2SiO_5 Polymorphs

FS Ohuchi, S Ghose
University of Washington, Seattle, Washington

Low–Angle, X-Ray Characterization of Catalyst Porosity

CF Habeger, M Delgado, XS Li
Pacific Northwest National Laboratory, Richland, Washington

XPS Characterization of Ion-Beam Induced Surface Modification

J Laskin, AK Shukla, E Denisov
Pacific Northwest National Laboratory, Richland, Washington

Fundamental Studies of Implantation Defects in 4H-SiC

Y Zhang
W.R. Wiley Environmental Molecular Sciences Laboratory, Richland, Washington

The Characterization of the Solid State Materials with Planar Carbon Cluster Unit

H Zhang
Washington State University, Richland, Washington

Interfacial Characterization of Self-Assembled Nanoparticle (SNAP) Film Deposited on Al and AA2024

MS Donley
University of Dayton, Dayton, Ohio
JA Johnson
Wright Patterson AFB/Nichols Research Corporation, Dayton, Ohio

Irradiation Effects in Pyrochlore Ceramics

BD Begg
Australian Nuclear Science and Technology Organization (ANSTO), Menai, NSW, Australia

SEM of Polyaniline/Fe-Hexacyanoferrate Composite Film

Y Lin
Pacific Northwest National Laboratory, Richland, Washington

Growth and Investigation of Co-Doped Anatase Films
U Diebold, K Katsiev, N Ruzycki
Tulane University, New Orleans, Louisiana

Microfabricated Series Connected Electro-Chemical Potentiometric Oxygen Sensor and Fuel Cell
R Radhakrishnan, AV Virkar
University of Utah, Salt Lake City, Utah
SC Singhal
Pacific Northwest National Laboratory, Richland, Washington

Bromine Etch Rates of P Type Solar Cell Absorbers and SEM, SEM Edax Studies on the Etched Material
PA Eschbach
Hewlett Packard, Corvallis, Oregon

Determination of Metal Dispersion Values
DL King
Pacific Northwest National Laboratory, Richland, Washington

Measurement of Carbon Cluster Emission from Graphite Sputtered By Noble Gas Ions Near Threshold
RE Stevens
Whitworth College, Spokane, Washington
AG Joly
Pacific Northwest National Laboratory, Richland, Washington

In-Situ, High-Temperature Oxidation Studies of FeCrAlY Metal
BR Johnson, CL Aardahl
Pacific Northwest National Laboratory, Richland, Washington

Single-Molecule Imaging at LB Bilayers
HP Lu, D Hu
Pacific Northwest National Laboratory, Richland, Washington

Accumulation of Chromium in *Shewanella oneidensis* MR-1
S Viamajala
Washington State University, Pullman, Washington

Influence of Calcium Carbonate Coatings on Contaminant Reactivity
TC Droubay
Pacific Northwest National Laboratory, Richland, Washington

Delphi Lithium Battery—2001
GW Coffey
Pacific Northwest National Laboratory, Richland, Washington

Strengthening Mechanisms in Ultra High Strength Corrosion Resistant Steel
WE Wood, G Nightingale, G Mares, J Keegan
Portland State University, Portland, Oregon

Supercritical Fluid Immersion Deposition of Metal Films on Semiconductor
X Ye
University of California San Diego, La Jolla, California

Design Fabrication and Testing of Series Connected Micro-Electrochemical Sensors
R Radhakrishnan, AV Virkar
University of Utah, Salt Lake City, Utah
SC Singhal
Pacific Northwest National Laboratory, Richland, Washington

Cu Interconnect Structure in the FESEM
DP Field, Y Kusama
Washington State University, Pullman, Washington

AES Study of Chemical Segregation in the Ti-Pt-PZT System for MEMS Devices
DF Bahr, LR Eakins
Washington State University, Pullman, Washington

Determining Mechanism of Pu(VI) Reduction by Manganese Oxides
KJ Cantrell
Pacific Northwest National Laboratory, Richland, Washington

Development of Novel Mass Spectrometry Instrumentation for Real-Time Monitoring of Trace Levels of Volatile Organic Compounds
PT Palmer, W Funk
San Francisco State University, San Francisco, California

Determination of the Factors Controlling Colloid Generation from Altered Waste Forms: TEM Study of Colloid Interactions and Fr Structure
EC Buck
Pacific Northwest National Laboratory, Richland, Washington

Accurate Size Measurement of Bacterium SAR-11
SJ Giovannoni
Oregon State University, Corvallis, Oregon

Microstructure Characterization of Pt on Si
BR Johnson
Pacific Northwest National Laboratory, Richland, Washington

New Metal Niobate and Silicotitanate Ion Exchangers: Development and Characterization

L Li
Pacific Northwest National Laboratory, Richland, Washington

Stable Isotopes to Study Nutrient Cycling in Soils

JB Cliff, DD Myrold, PJ Bottomley
Oregon State University, Corvalis, Oregon
DJ Gaspar
W.R. Wiley Environmental Molecular Sciences Laboratory, Richland, Washington

Sea Urchin Biomineralization: A Secondary Ion Mass Spectroscopy (SIMS) Analysis

JM Seto, FH Wilt, G Vrdoljak
Lawrence Berkeley National Laboratory, University of California, Berkeley, Berkeley, California

The Surface Chemistry of Iron Metal in Environmental Remediation Applications

PG Tratnyek
Oregon Health Sciences University/Oregon Graduate Institute, Beaverton, Oregon

TEM Study of Strontium Bismuth Niobate Ferroelectric Ceramics Doped with Vanadium and Tungsten Oxides

G Cao, SJ Limmer
University of Washington, Seattle, Washington

Evaluation of Multicomponent Porous Oxide Films

XS Li
Pacific Northwest National Laboratory, Richland, Washington

Characterization of Aluminosilicate Phases Forming Under Low-Silica Conditions

S Mattigod
Pacific Northwest National Laboratory, Richland, Washington

Synthesis, Characterization and Testing of Novel Materials for Plasma-Catalyst Technology

C Lee, S Noh, H Lee, H Choi, S Kim, H Kim
Keimyung University, Dalseo-Gu, Republic of Korea

Application of Ion Trap Mass Spectrometry for Analysis of Diesel Exhaust Emissions

MR Smith
Pacific Northwest National Laboratory, Richland, Washington

Spectroscopy and Microscopy of Doped TiO_2 Nanocrystalline Materials

DR Gamelin, JD Bryan, P Radovanovic, NS Norberg
University of Washington, Seattle, Washington

Fuel Reforming Catalyst Characterization
PM Irving, Q Ming
Innovateck, Inc., Richland, Washington

Determination of Valance Band Offset in $Sr_2TiO_4/SrTiO_3$ Heterostructures
JH Haeni, DG Schlom
Pennsylvania State University, University Park, Pennsylvania

Investigation of Oxidation State of Elements in Natural Brannerites
MX Colella
Australian Nuclear Science and Technology Organization (ANSTO),
Lucas Heights, Australia
EC Buck
Pacific Northwest National Laboratory, Richland, Washington

Fundamental Studies of Monolayer-Protected Nanoparticles by Gas Chromatography
RE Synovec, GM Gross
University of Washington, Seattle, Washington
JW Grate
Pacific Northwest National Laboratory, Richland, Washington

Epitaxial Growth and Properties of Nanoscale Oxides for Spintronics
D Schmidt, FS Ohuchi, M Olmstead
University of Washington, Seattle, Washington

Advanced Actuator Materials Based on Carbon Nanotube Composites
LS Fifield, CL Aardahl
Pacific Northwest National Laboratory, Richland, Washington

Interfacing Chip-Based Nanofluidic Systems to Surface Desorption Mass Spectrometry
JS Kuo, G Fiorini, DT Chiu
University of Washington, Seattle, Washington

White Layer Characterization
WE Wood, J Keegan
Portland State University, Portland, Oregon

Dilute Magnetic Semiconducting Oxide Thin Films and Nanostructures
K Krishnan, GP Blomqvist, A Pakhomov
University of Washington, Seattle, Washington

Characterization of Sn Whiskers
MG Norton, JB LeBret
Washington State University, Pullman, Washington

Growth of MOCVD ZnO on CIGSS Solar Cells

SN Kundu
Washington State University, Tri-Cities, Richland, Washington

Texture Studies of Aluminum Extrusion

VY Guertsman
Pacific Northwest National Laboratory, Richland, Washington

SIMS Analysis of Nickel-Silicon Multilayers

DC Johnson, J Jensen
University of Oregon, Eugene, Oregon

How Desert Varnish Forms

RS Perry, JT Staley, RS Sletten
University of Washington, Seattle, Washington
V Kolb
University of Wisconsin-Parkside, Kenosha, Wisconsin

MeV Ion Irradiation of Non-Ice Solar System Analogue Materials

CA Hibbitts, TB McCord, GB Hansen
University of Washington, Seattle, Washington

Characterization of Nanocomposites Using Electrochemistry, XPS, TEM, and SEM

X Ye
University of California San Diego, La Jolla, California

Investigating Electrochemical Properties, Composition, and Oxidation States of Nanoparticles and Catalysts Using Electrochemist XPS

C Zhong
State University of New York at Binghamton, Binghamton, New York

Exchange Bias in Fe/MnPd Bilayers

GP Blomqvist, X Ji, K Krishnan
University of Washington, Seattle, Washington

Development of a Capability to Quantify Arsenic in an Adsorbent

S Maheswaran, NN Yadav
University of Western Sydney, Nepean Australia, Penrith South DC, Australia

Automated Suspension Microarray for Microbial Community Profiling

DP Chandler
Argonne National Laboratory, Argonne, Illinois
AE Jarrell
Pacific Northwest National Laboratory, Richland, Washington

Growth and Characterization of Fe Doped TiO_2 Films

YJ Kim
Hanbat National University (formerly Taejon National University of Technology), Vancouver, Canada

X-Ray Diffraction and Transmission Electron Microscopy Measurements of Cobalt Nanospheres, Disks, and Rods

M Beerman
University of Washington, Seattle, Washington

Determination of Size Distribution of Thermal Spray Powders and Tungsten Carbide Particle Size and Distribution Present in Powders

DG Atteridge
Columbia Basin College, Pasco, Washington
GA Tewksbury
Oregon Health Sciences University/Oregon Graduate Institute, Beaverton, Oregon

A Combinatorial Sputtering Approach to Properties Modification in Polaron Conducting Films

RR Owings, PH Holloway
University of Florida, Gainesville, Florida

Microstructural and Microchemical Analysis of Chalcogenide Nanowires

BR Johnson
Pacific Northwest National Laboratory, Richland, Washington

Microstructural and Microchemical Analysis of Catalysts

BR Johnson
Pacific Northwest National Laboratory, Richland, Washington

Trace Measurements of Organics Due to Pyrolysis of Jet Engine Turbine Oil

CE Bick, VG Johnston, J Ray
Boeing, Seattle, Washington
ML Alexander, BT Jobson
Pacific Northwest National Laboratory, Richland, Washington

Mixed Alkali Effect on Oxidation of Si_3N_4: A Compositional Study Using RBS

HH Du
Stevens Institute of Technology, Hoboken, New Jersey

Preparing Specimens for the Scanning Electron Microscope

JB Von Reis, AL Matthiessen, RE Fox, JE Frazier, A Huffman
Columbia Basin College, Pasco, Washington

Reactivity of Primary Soil Minerals and Secondary Precipitates Beneath Leaking Hanford Waste Tanks

W Um
Pacific Northwest National Laboratory, Richland, Washington

Use of EMSL Scanning Microscopy Capabilities to Study Soil Mineral Weathering

Z Balogh, J Dickinson, CK Keller, AL Espana
Washington State University, Pullman, Washington

SEM of Life Stages of Gall Wasps of the Family *Cynipidae*

JD DeMartini
Humboldt State University, Arcata, California

AFM and XPS Corrosion Research on Rock Bolt for Yucca Mountain Repository

D Chandra, V Deodeshmukh
University of Nevada, Reno, Reno, Nevada

Evaluation of Cold Cap Reaction Layer in a High-Level Waste Melter for DOE Tank Wastes

J Matyas
Pacific Northwest National Laboratory, Richland, Washington

Chemical State Image Analysis of Biologically Relevant Patterned Surfaces

B Wickes, DG Castner
University of Washington, Seattle, Washington

Magnetics Nanoparticles Characterization

Y Bao
University of Washington, Seattle, Washington

XPS Characterization of Hydroquinone-Treated Hematite

CM Eggleston
University of Wyoming, Laramie, Wyoming
AG Stack
University of California Davis, Davis, California

SEM Image Acquisition, X-Ray Elemental Analysis

RM Ozanich
Pacific Northwest National Laboratory, Richland, Washington

Long-Term Monitoring of Permeable Reactive Barriers

W Kamolpornwijit
Oak Ridge National Laboratory, Oak Ridge, Tennessee

Characterization of Advanced Materials: A Summer 2002 Research Experience for Undergraduates

AH Backstrom, DF Bahr, MG Norton, AD LaLonde, PR Leroueil, BD Matson, A Cumberlidge, HH Doodnauth, SA Bernard, MA Turner, CC Harris, SC Pevov, BS McDonald, KL Calvert, ST Lovald
Washington State University, Pullman, Washington

Morphology of Colloids Formed in Soils Reacted with Simulated Hanford Waste Tank Solutions and the Distribution of Incorporated Adsorbed Cesium in the Colloids

Y Deng, JB Harsh, M Flury
Washington State University, Pullman, Washington

Reaction Specificity of Nanoparticles in Solution

Y Qiang
University of Idaho, Moscow, Idaho
RL Penn
University of Minnesota, Minneapolis, Minnesota
PG Tratnye
Oregon Health Sciences University/Oregon Graduate Institute, Beaverton, Oregon
A El-Azab, DR Baer, KH Pecher, JE Amonette, EJ Bylaska, BD Kay, M Dupuis
Pacific Northwest National Laboratory, Richland, Washington

Cooperation on Nanocomposite Materials Using PNNL/EMSL User Facilities

K Jiang, R Siegel, LS Schadler
Rensselaer Polytechnic Institute, Troy, New York

ESEM Evaluation of MIC in Steel Fittings

BJ Little
Stennis Space Center, Diamondhead, Mississippi

Hematite Thin Film Preparation for X-Ray Spectroscopic Studies of the Reactivity and Distribution of Pb(II) and As(V) at Natural or Matter/Iron Oxide Interfaces

T Yoon, GE Brown
Stanford University, Palo Alto, California

TEM Use for Analysis of Base Glasses and Doped Glasses

LA Rogers
Massachusetts Institute of Technology, Cambridge, Massachusetts

Assessment of TRI Chemical Emisson Factors from Munitions by Real-Time Mass Spectrometric Air Monitoring

BT Jobson, ML Alexander
Pacific Northwest National Laboratory, Richland, Washington
CW Spicer
Battelle Columbus, Columbus, Ohio

Texture, Morphology, and Stress in PZT Thin Films

DF Bahr, AL Olson, MS Kennedy, JV Martinez, MC Robinson
Washington State University, Pullman, Washington

Uranium(VI) Sorption onto Hematite Surfaces

D Bosbach, K Dardenne, M Denecke
Forschungszentrum Karlsruhe, Institute for Nuclear Waste Management,
Karlsruhe, Germany

Confirmation of Si-C Bonds in Grafted Monolayer through XPS

CD Struckman
South Dakota School of Mines and Technology, Rapid City, South Dakota

Plasma Mechanisms for the Deactivation of Bacterial Spores

JG Birmingham
MicroEnergy Technologies, Inc., Vancouver, Washington

Experimental Measurements of the Band Offsets of Epitaxial Silicon on $LaAlO_3$ Single Crystals

LF Edge, DG Schlom, V Vaithyanathan
Pennsylvania State University, University Park, Pennsylvania
SA Chambers
Pacific Northwest National Laboratory, Richland, Washington

Structural Characterizations of Biogenic Germanium Oxide Nanospheres

C Chang, G Rorrer, S Liu
Oregon State University, Corvallis, Oregon

GLAD Coating Microstructure

D Matson
Pacific Northwest National Laboratory, Richland, Washington

Determination of the Bonding of Various Surfactants onto ZrW_2O_8

ED Swanson
South Dakota School of Mines and Technology, Rapid City, South Dakota

Using Ni-Ion Irradiation for the Development of Advanced Materials for the Next Generation Nuclear Reactor

J Gan, TR Allen
Argonne National Laboratory-West, Idaho Falls, Idaho

Characterization of Defects in Nd:YAG Using High-Resolution Transmission Electron Microscopy

DE Eakins, MG Norton
Washington State University, Pullman, Washington

Hydrolytic Stability and Susceptibility of Transition Metal Diolate Complexes and Applications to Green Oxidation

KP Gable
Oregon State University, Corvallis, Oregon

Epoxy-Zirconate Sol-Gel Studies

LS Kasten, MS Donley
University of Dayton, Dayton, Ohio

Flux Measurements of Biogenic Volatile Organic Compounds by Disjunct Eddy Sampling and Ion Trap Mass Spectrometry Analysis

D Helmig, JV Ortega
University of Colorado, Boulder, Colorado

A Theoretical and Experimental Investigation of Multiplet Splitting for Cr Spectra Generated by X-Ray Photoelectron Spectroscopy

PS Bagus
University of North Texas, Denton, Texas
ES Ilton
Pacific Northwest National Laboratory, Richland, Washington

Molecular Beam Epitaxy Growth of Barium Strontium Titanate

TC Kaspar
University of Washington, Seattle, Washington
JW Rogers
W.R. Wiley Environmental Molecular Sciences Laboratory, Richland, Washington

XPS Analysis of Oxidized Metal Surface

BR Johnson, Y Chin
Pacific Northwest National Laboratory, Richland, Washington

Studies of the Effect of Particle Size on LA/ICP/MS of Heterogeneous Samples

BW Smith, JD Gutierrez, JD Winefordner
University of Florida, Gainesville, Florida

Characterization of Mn Oxidation State with Electron Energy Loss Spectroscopy

EC Buck
Pacific Northwest National Laboratory, Richland, Washington

Three-Dimensional Imaging of the Photosynthetic Bacterium, *Rhodobacter sphaeroides*

RC Mackenzie
University of Texas Health Science Center at Houston, Houston, Texas

Task 1– Residual Characterization

DJ Hymes
LAM Research Corporation, Fremont, California

Fabrication of Nanoelectrode Array Base on Aligned Carbon Nanotube

Y Tu, Z Ren
Boston College, Chestnut Hill, Massachusetts

Oxidation Studies of Coatings for Interconnect Plates in Solid Oxide Fuel Cells

CV Ramana, RJ Smith
Montana State University, Bozeman, Montana

Nuclear Reaction Analysis of Helium Retention in 6H SiC as a Function of Irradiation and Annealing

RJ Smith
Montana State University, Bozeman, Montana

Metallurgical Characterization of Coatings Deposited by Electrospark Deposition

J Keegan, WE Wood
Portland State University, Portland, Oregon
GA Tewksbury
Oregon Health Sciences University/Oregon Graduate Institute, Beaverton, Oregon

Changes of Surface Area of Diesel Soot as a Function of Oxidation

D Kim
Pacific Northwest National Laboratory, Richland, Washington

Catalyst Development for Microreactors

PE Gannon
Montana State University, Bozeman, Montana
DR Palo
Pacific Northwest National Laboratory, Richland, Washington

Electrochemical Sensors for Pesticides and Toxic Metals

F Lu
InTec Science, Inc., Brisbane, California

The Synthesis and Characterization of One-Dimensional Nanostructures

H Zhang, LN Wang
Washington State University, Richland, Washington

Solid Phase Transformations in the Hanford Sediments Treated with Al-Rich, Hyperalkaline and Saline Solutions

NP Qafoku
Pacific Northwest National Laboratory, Richland, Washington

Immobilized Enzymes for Bioremediation and Biosensing

H Jia
University of Akron, Akron, Ohio
TE Herricks
University of Washington, Seattle, Washington

J Lee, C Lee, K Min, S Chung
Seoul National University, Seoul, Republic of Korea
M Kim
Korea Advanced Institute of Science and Technology, Daejeon, Republic of Korea
J Kim, JW Grate
Pacific Northwest National Laboratory, Richland, Washington

Joint Catalyst Development

B Liang
Sichuan University, Chengdu, China

Laminar Growth of Ultrathin Metal Films on Oxide Surfaces

J Osterwalder
Universitaet Zuerich-Irchel, Zuerich, Switzerland

Characterization of Biologically Reduced Uranium Particles

BM Peyton, RK Sani
Washington State University, Pullman, Washington

Environmental Scanning Electron Microscopic Analysis of Gas Hydrate and Hydrate-Bearing Sediments

BP McGrail
Pacific Northwest National Laboratory, Richland, Washington
JS Young
W.R. Wiley Environmental Molecular Sciences Laboratory, Richland, Washington

Background Signal Studies with PTR-MS

HH Westberg
Washington State University, Pullman, Washington

SEM on Electrode Surface

W Yantasee
Pacific Northwest National Laboratory, Richland, Washington

Evaluate the Surface Chemistry of Two PVDF Polymers by XPS

LR Pederson
Pacific Northwest National Laboratory, Richland, Washington

Patterned Deposition of Chalcogenide Thin Films

F Zheng, BR Johnson, SK Sundaram, JE Martinez, BJ Riley
Pacific Northwest National Laboratory, Richland, Washington

Measurements for Nano-Tip 'ID

R Zhao
W.R. Wiley Environmental Molecular Sciences Laboratory, Richland, Washington

Carbon Nanomaterial Characterization

AS Blutke
Thermal Conversion, Corp. (TCC), Richland, Washington
JM Henderson
Nuvotec, Inc., Richland, Washington

Modified Carbon Supports for Aqueous Phase Catalysis: Applications for the Conversion of Glucose and Fermentation Products to Value-Added Chemicals

G Fryxell, JF White, JG Frye
Pacific Northwest National Laboratory, Richland, Washington

Characterization of Defects in Yttrium Orthovanadate

JB LeBret, MG Norton, JP Winterstein
Washington State University, Pullman, Washington

Development of Catalyst and Membrane Systems for Fuel Processing

PM Irving, Q Ming, HA Edberg
Innovateck, Inc., Richland, Washington

Synthesis and Analysis of Organic Hydroperoxide by PTR-MS

TG Karl
National Center for Atmospheric Research, Boulder, Colorado
ML Alexander, TL Hubler, BT Jobson
Pacific Northwest National Laboratory, Richland, Washington

Scanning Probe Microscope Observation of Anatase TiO_2 Films

H Onishi
Kanagawa Academy of Science and Technology, Takatsu-ku, Kawasaki-shi, Japan

SEM And SIMS Analysis of Organic Semiconductor Films Grown Using Liquid Crystal Solvents

DL Patrick, J McLellan
Western Washington University, Bellingham, Washington

Membrane Introduction Proton Transfer Reaction Mass Spectrometry

E Boscaini
University of Innsbruck, Innsbruck, Austria

Determination of the Structure and Properties of $NaAlH_4$ Hydrogen Storage Materials

A El-Azab
Pacific Northwest National Laboratory, Richland, Washington

Characterization of Heat Treated Silicon Carbide Specimens Using Scanning Electron Microscopy

MJ Guinel, MG Norton
Washington State University, Pullman, Washington

XPS Characterization of the Passive Film/Corrosion Products Formed on Carbon Steel and Ni-Base Alloy in the Yucca Mountain Repository Environment

V Arjunan, J Lamb
University of Nevada, Reno, Reno, Nevada

Characterizing Metal Nanoparticle Nanoassemblies

SR Emory, HR Pugsley
Western Washington University, Bellingham, Washington

Electrochemical Sensor for Environmental Monitoring of Pesticides and Toxic Metals

L Bi
Jilin University, Changchun, China

Novel Structures in Nanocrystalline Ceramic Materials

G Zhan
University of California Davis, Davis, California

High-Resolution Transmission Electron Microscopic Evidences of Stacking Faults in Zeolitic Minerals Formed in Hanford Sediments with Simulated Tank Waste Solutions

Y Deng
Washington State University, Pullman, Washington

Microbial Biosignatures in Ocean Basalts

MR Fisk, JA Josef
Oregon State University, Corvallis, Oregon

Diffusion Study of α-Fe_2O_3/A-Cr_2O_3(0001) Superlattice

DC Johnson, TM Phung
University of Oregon, Eugene, Oregon

Probing the Origin of the Photo-Induced Hydrophilicity on TiO_2

JM White
University of Texas at Austin, Austin, Texas

SEM Characterization of Engineered Forms of SAMMS

S Mattigod
Pacific Northwest National Laboratory, Richland, Washington

Microelectromagnets

G Dunham
Pacific Northwest National Laboratory, Richland, Washington

Differential Anomalous Scattering Determination of Co in Anatase in Co-Doped TiO_2

MF Toney
Stanford Linear Accelerator Center, Menlo Park, California

Nanoclusters, Nanomaterials, and Nanotechnology

J Antony
University of Idaho, Moscow, Idaho
Q Liu
Florida State University, Tallahassee, Florida
A El-Azab, DR Baer
Pacific Northwest National Laboratory, Richland, Washington

EM Analysis of Bacterial Co-Cultures

FJ Brockman
Pacific Northwest National Laboratory, Richland, Washington

On-Line Determination of Selected Vapor-Phase Hoffmann List Compounds by PTR-MS

GM Anderson
Washington State University, Tri-Cities, Richland, Washington

Image Iron Oxide Nanoparticles

GR Holtom
W.R. Wiley Environmental Molecular Sciences Laboratory, Richland, Washington

DC-1 Molecular and Bio Imprinting

XS Li
Pacific Northwest National Laboratory, Richland, Washington

Silicon Carbide Nanowires and Nanosprings: Processing, Self-Assembly, Characterization, and Properties

D Zhang, DN McIlroy, AI Alkhateeb, J Wei, YA Kranov, H Mahood
University of Idaho, Moscow, Idaho
AD LaLonde
Washington State University, Pullman, Washington

Two-Dimensional Photonic Crystals Grown by Atomic Layer Deposition for Near-IR and Visible-Optoelectronics Applications

D Zhang, DN McIlroy, AI Alkhateeb, J Wei, YA Kranov, H Mahood
University of Idaho, Moscow, Idaho
AD LaLonde
Washington State University, Pullman, Washington

Mechanisms of Sulfur Poisoning of NOx Adsorber Materials

Y Chin
Pacific Northwest National Laboratory, Richland, Washington

Determine Particle Morphology in Ultrasound Assisted Heterogeneous Catalysis

RS Disselkamp
Pacific Northwest National Laboratory, Richland, Washington

Ion-Solid Interactions in Ceramics

WJ Weber, W Jiang
Pacific Northwest National Laboratory, Richland, Washington

Materials and Methods for Multivariate Chemical Vapor Sensing

JW Grate, DL Baldwin, NC Anheier
Pacific Northwest National Laboratory, Richland, Washington

Monolayer Protected Gold Nanoparticle Investigation and Characterization

JW Grate, BP Dockendorff
Pacific Northwest National Laboratory, Richland, Washington
LA Hughes
Southern Oregon University, Ashland, Oregon

Synthesis and Characterization of Novel Nanocrystalline Oxide Film Structures: Interface Controlled, Self-Assembled Oxide Quantum

JF Groves, Y Du
University of Virginia, Charlottesville, Virginia
A El-Azab, CF Windisch, DR Baer, J Szanyi
Pacific Northwest National Laboratory, Richland, Washington

TEM Study of Carbon Nanotube Reinforced Polymer-Derived Ceramic Composites

L An
University of Central Florida, Orlando, Florida

PTR-MS Characterization of Carbon Nanotube Preconcentrators for Trace Chemical Signature Detection

F Zheng
Pacific Northwest National Laboratory, Richland, Washington

Low Energy Sputtering Experiments using RBS

MR Nakles, MT Domonkos
National Aeornautics and Space Administration, Glenn Research Center, Cleveland, Ohio

Characterization of Noble Metal Catalysts for Hydrogen Production and Purification in Fuel Cell Applications

S Chin, MD Amiridis
University of South Carolina, Columbia, South Carolina

Hydrogen Adsorption Characterization of Carbon Supported Catalyst

F Zheng
Pacific Northwest National Laboratory, Richland, Washington

Characterization Polymer Thin Films and Arrays

M Yan, J Ren, R Joshi, MB Harnish
Portland State University, Portland, Oregon
Y Chen
Oregon Health Sciences University/Oregon Graduate Institute, Beaverton, Oregon

Fabricate Nanoscale Thin Film Cathode with Sputter Deposition

Y Lu, S Adler, JR Wilson, L Dunyushkina
University of Washington, Seattle, Washington
O Marina
Pacific Northwest National Laboratory, Richland, Washington

Steam Reforming of Methanol Over a Highly Active and Selective Pd/ZnO Catalyst

RA Dagle
Pacific Northwest National Laboratory, Richland, Washington

Mechanisms for Self Healing in Gastropods: Lessons from Biology, a Case Study of Two Species, *Lavigeria grandis* and *Nucella lamellosa*

KM Hinkley
University of Washington, Bellevue, Washington

Field Effect Studies of $Co_xTi_{1-x}O_2$ Thin Films

AS Posadas, J Yau, C Ahn
Yale University, New Haven, Connecticut

TeO_2 Detector Surfaces

FT Avignone
University of South Carolina, Columbia, South Carolina

Particle Size, Associations, and Crystallinity of Bioreduced Uranium Phases

S Fendorf, JM Neiss
Stanford University, Palo Alto, California

Real Time Trace Gas Measurements by Chemical Ionization Mass Spectrometry

MV White
Sacramento City College, Sacramento, California
BT Jobson, ML Alexander
Pacific Northwest National Laboratory, Richland, Washington

Elemental Analysis of Bulk Aerosol Samples Collected with a Drum Impactor During the MCMA 2003 Field Study

MJ Molina, BM Zuberi, KS Johnson
Massachusetts Institute of Technology, Cambridge, Massachusetts
RS Disselkamp, AB Laskin
Pacific Northwest National Laboratory, Richland, Washington

Continuous Isosorbide Production

JE Holladay
Pacific Northwest National Laboratory, Richland, Washington

TGA/DSC Analysis of Anhydrosugar Samples

JE Holladay
Pacific Northwest National Laboratory, Richland, Washington

New Technologies for Reduction of Automobile Exhaust Emissions

H Zhao
University of Southern California, Los Angeles, California
CH Peden
Pacific Northwest National Laboratory, Richland

Silicon Nanotips for Enhanced Electron Emission

G Dunham, CC McQuerry
Pacific Northwest National Laboratory, Richland, Washington

Bioavailability of Arsenic in Dislodgeable Residue from Pressure-Treated Wood

BM Sass
Battelle Columbus, Columbus, Ohio

Photovoltaics Projects

G Fryxell
Pacific Northwest National Laboratory, Richland, Washington

XPS Characterization of Diesel Soot Materials

D Kim
Pacific Northwest National Laboratory, Richland, Washington

Electrochemical and AFM/STM Study of TiO_2 (Anatase) Film on $SrTiO_3$ Substrate

L Kavan
J. Heyrovsky Institute of Physical Chemistry, Academy of Sciences of the Czech Republic,
Prague, Czech Republic

Oxydation of Fe/Cu and Fe/Ag Multilayer Films Prepared by DC Magnetron Sputtering

AP Kouprine, DU Ryan, Z Altounian
McGill University, Montreal, Quebec, Canada

Characterization of Regenerable CO_2 Sorbents

F Zheng
Pacific Northwest National Laboratory, Richland, Washington

Chemical Processing of Terpene Emissions from Forests

PV Doskey
Argonne National Laboratory, Argonne, Illinois

Europium Uptake in Various SAM Coated Mesoporous Silica

JT Bays
U.S. Military Academy, West Point, New York
RS Addleman, ED Bott
Pacific Northwest National Laboratory, Richland, Washington

TEM and XPS Analysis of Ligand-Functionalized Semiconductor Quantum Dots Used in Biodetection Studies

MG Warner, C Bruckner-Lea
Pacific Northwest National Laboratory, Richland, Washington

Phenotypic Characterization of TCE and PCE Degrading Dehalococcoides

MR Fisk, AR Sabalowsky, LC Semprini, LB Parker, NW Chambers
Oregon State University, Corvallis, Oregon

Degradation of Oxalate Containing Compounds by Soil Microbes

SA Boyle, DD Myrold
Oregon State University, Corvallis, Oregon

Physical Properties of Natural Siliceous Sinters from Thermal Springs

NW Hinman
University of Montana, Missoula, Montana

Surface Structure and Chemistry of Carbonate Minerals

DR Baer, JE Amonette
Pacific Northwest National Laboratory, Richland, Washington

Ultrapure, Monodisperse, Spherical, Unagglomerated Nano Powders for Infrared Window Materials

A Akash
Ceramatec, Inc., Salt Lake City, Utah

Hydrogen Adsorption/Release Study of Selected Chemical Hydrides

L Li
Pacific Northwest National Laboratory, Richland, Washington

Investigation of Strain in Ingan MQW Structures

MC Johnson
Lawrence Berkeley National Laboratory, University of California, Berkeley,
Berkeley, California

Oxidation of Lead Sulfide Surfaces in the Presence of Phosphate: Nanoparticle Formation

AG Stack, WH Casey
University of California at Davis, Davis, California

TEM and SEM Investigation of Non-Pathogenic Bacterial Cultures

AC Dohnalkova

Pacific Northwest National Laboratory, Richland, Washington

Variable Temperature XRD Studies of Ge/SiO_2/Si Systems

Y Liang

Motorola, Inc., Tempe, Arizona

Observations of Scytonema-Colonized and Non-Colonized Fiber Cement Roofing Shingles

RM Fisher, BA Reine

Lab/Cor, Inc., Seattle, Washington

Magnetic and Transport Studies of Co Doped TiO_2 Thin Films

A Punnoose

Boise State University, Boise, Idaho

Composition Characterization of ZnO:Cr and ZnO:Co

BK Roberts, K Krishnan

University of Washington, Seattle, Washington

MBE Growth of Epitaxial Anatase TiO_2(001) on STO(001) and Si(001) and Characterization of TiO_2 Films

KA Griffin, K Krishnan

University of Washington, Seattle, Washington

Fabrication and Characterization of Functional Nanostructured Materials

S Jin, X Ye

University of California at San Diego, La Jolla, California

Fabrication and Characterization of Carbon Nanotube-Based Composites

S Jin, X Ye

University of California at San Diego, La Jolla, California

Synthesis and Characterization at Atomic Level of Novel Nanocrystalline Metal Oxide Structures

Z Yu

Nanjing Normal University, Nanjing, China

Analysis of Catalysts and Microchannel Components

VS Stenkamp, KP Brooks, DL King, W Tegrotenhuis, CM Fischer

Pacific Northwest National Laboratory, Richland, Washington

Template-Based Growth of V_2O_5 Nanorods by Electrodeposition and/or Sol Electrophoresis

SJ Limmer, G Cao
University of Washington, Seattle, Washington

STM Tip Analysis by TEM

Z Dohnalek
Pacific Northwest National Laboratory, Richland, Washington

Micro-Dimension Calibration

YB Peng
XL Science & Technology, Richland, Washington

Sulfur Absorbents for Emission Control

L Li
Pacific Northwest National Laboratory, Richland, Washington

The Synthesis of Au Nanoclusters

H Zhang, LN Wang
Washington State University, Richland, Washington

Development of a Soldier-Portable Power System

DR Palo
Pacific Northwest National Laboratory, Richland, Washington

Characterization of Surface and Materials

C Lei
Pacific Northwest National Laboratory, Richland, Washington

SEM Characterization of Proposed Hydrogen Storage Materials

LE Thomas
Pacific Northwest National Laboratory, Richland, Washington

XPS Analysis of Fuel Cell Components

LR Pederson
Pacific Northwest National Laboratory, Richland, Washington

Investigation of Elemental Contamination in Solid Oxide Fuel Cell Materials

VL Sprenkle
Pacific Northwest National Laboratory, Richland, Washington

Analysis of Catalysts

DC Elliott
Pacific Northwest National Laboratory, Richland, Washington

Growth of Vanadium Oxides on Anatase $TiO_2(001)$

W Gao, EI Altman
Yale University, New Haven, Connecticut

Chalcogenide Surface Science

BR Johnson
Pacific Northwest National Laboratory, Richland, Washington

Deposition of Cobalt-Doped Oxides for Spintronic Applications

TC Kaspar, SA Chambers, TC Droubay
Pacific Northwest National Laboratory, Richland, Washington

Continuous Liquid Feed Flash Evaporation System for Organic Semiconductors

PE Burrows
Pacific Northwest National Laboratory, Richland, Washington

Influence of Gd and Sm Doping on Atomic and Ionic Transport Properties of Novel Nanostructured Ceria-Zirconia Multilayers

A El-Azab, O Marina, D Matson
Pacific Northwest National Laboratory, Richland, Washington
T Thevuthasan
W.R. Wiley Environmental Molecular Sciences Laboratory, Richland, Washington

Staff

S. Thevuthasan, Senior Research Scientist, Technical Lead
(509) 376-1375, theva@pnl.gov

Lisa Smith, Senior Administrative Secretary
(509) 376-1518, l.smith@pnl.gov

Mark H. Engelhard, Research Scientist
(509) 376-1664, mark.engelhard@pnl.gov

Daniel J. Gaspar, Senior Research Scientist
(509) 376-2413, daniel.gaspar@pnl.gov

A. Scott Lea, Senior Research Scientist
(509) 376-9145, scott.lea@pnl.gov

Igor V. Lyubinetsky, Senior Research Scientist
(509) 376-5220, igor.lyubinetsky@pnl.gov

David E. McCready, Research Scientist
(509) 376-9648, david.mccready@pnl.gov

Matthew I. McKinley, Student
(509) 376-1117, matthew.mckinley@pnl.gov

Laxmikant V. Saraf, Senior Research Scientist
(509) 376-2006, laxmikant.saraf@pnl.gov

V. Shutthanandan, Senior Research Scientist
(509) 376-2708, shuttha@pnl.gov

Casey C. Stratton, Student
(509) 376-2539, casey.stratton@pnl.gov

Chongmin M. Wang, Senior Research Scientist
(509) 376-4292, chongmin.wang@pnl.gov

James S. Young, Technologist
(509) 376-2046, jim.young@pnl.gov

Yanwen Zhang, Senior Research Scientist
(509) 376-3429, yanwen.zhang@pnl.gov